A&A 517, A85 (2010)
DOI: 10.1051/0004-6361/201014156

Astronomy & Astrophysics

Massive star formation in Wolf-Rayet galaxies⋆,⋆⋆

IV. Colours, chemical-composition analysis and metallicity–luminosity relations

Á. R. López-Sánchez[1,2] and C. Esteban[2,3]

[1] CSIRO Astronomy & Space Science / Australia Telescope National Facility, PO BOX 76, Epping, NSW 1710, Australia
e-mail: Angel.Lopez-Sanchez@csiro.au
[2] Instituto de Astrofísica de Canarias, C/ Vía Láctea S/N, 38200 La Laguna, Tenerife, Spain
[3] Departamento de Astrofísica de la Universidad de La Laguna, 38071 La Laguna, Tenerife, Spain

Received 29 January 2010 / Accepted 18 March 2010

ABSTRACT

Aims. We have performed a comprehensive multiwavelength analysis of a sample of 20 starburst galaxies that show a substantial population of very young massive stars, most of them classified as Wolf-Rayet (WR) galaxies. In this paper, the forth of the series, we present the global analysis of the derived photometric and chemical properties.

Methods. We compare optical/*NIR* colours and the physical properties (reddening coefficient, equivalent widths of the emission and underlying absorption lines, ionization degree, electron density, and electron temperature) and chemical properties (oxygen abundances and N/O, S/O, Ne/O, Ar/O, and Fe/O ratios) with previous observations and galaxy evolution models. We compile 41 independent star-forming regions – with oxygen abundances between 12 + log(O/H) = 7.58 and 8.75 – , of which 31 have a direct estimate of the electron temperature of the ionized gas.

Results. According to their absolute *B*-magnitude, many of them are not dwarf galaxies, but they should be during their quiescent phase. We found that both $c(\mathrm{H}\beta)$ and W_{abs} increase with increasing metallicity. The differences in the N/O ratio is explained assuming differences in the star formation histories. We detected a high N/O ratio in objects showing strong WR features (HCG 31 AC, UM 420, IRAS 0828+2816, III Zw 107, ESO 566-8 and NGC 5253). The ejecta of the WR stars may be the origin of the N enrichment in these galaxies. We compared the abundances provided by the direct method with those obtained through empirical calibrations, finding that (i) the Pilyugin method is the best suited empirical calibration for these star-forming galaxies; (ii) the relations provided by Pettini & Pagel (2004, MNRAS, 348, 59) give acceptable results for objects with 12 + log(O/H) > 8.0; and (iii) the results provided by empirical calibrations based on photoionization models are systematically 0.2–0.3 dex higher than the values derived from the direct method. The O and N abundances and the N/O ratios are clearly related to the optical/*NIR* luminosity; the dispersion of the data is a consequence of the differences in the star-formation histories. The *L*–*Z* relations tend to be tighter when using *NIR* luminosities, which facilitates distinguishing tidal dwarf galaxies candidates and pre-existing dwarf objects. Galaxies with redder colours tend to have higher oxygen and nitrogen abundances.

Conclusions. Our detailed analysis is fundamental to understand the nature of galaxies that show strong starbursts, as well as to know their star formation history and the relationships with the environment. This study is complementary –but usually more powerful– to the less detailed analysis of large galaxy samples that are very common nowadays.

Key words. galaxies: starburst – galaxies: interactions – galaxies: dwarf – galaxies: abundances – galaxies: photometry – stars: Wolf-Rayet

1. Introduction

The knowledge of the chemical composition of galaxies, in particular of dwarf galaxies, is vital for understanding their evolution, star formation history, stellar nucleosynthesis, the importance of gas inflow and outflow, and the enrichment of the intergalactic medium. Indeed, metallicity is a key ingredient for modelling galaxy properties, because it determines *UV*, optical and *NIR* colours at a given age (i.e., Leitherer et al. 1999), nucleosynthetic yields (e.g., Woosley & Weaver 1995), the dust-to-gas ratio (e.g., Hirashita et al. 2001), the shape of the interstellar extinction curve (e.g., Piovan et al. 2006), or even the properties of the Wolf-Rayet stars (Crowther 2007).

The most robust method to derive the metallicity in star-forming and starburst galaxies is via the estimate of metal abundances and abundance ratios, in particular through the determination of the gas-phase oxygen abundance and the nitrogen-to-oxygen ratio. The relationships between current metallicity and other galaxy parameters, such as colours, luminosity, neutral gas content, star-formation rate, extinction or total mass, constrain galaxy-evolution models and give clues about the current stage of a galaxy. For example, is still debated whether massive star formation results in the instantaneous enrichment of the interstellar medium of a dwarf galaxy, or if the bulk of the newly synthesized heavy elements must cool before becoming part of

⋆ Based on observations made with NOT (Nordic Optical Telescope), INT (Isaac Newton Telescope) and WHT (William Herschel Telescope) operated on the island of La Palma jointly by Denmark, Finland, Iceland, Norway and Sweden (NOT) or the Isaac Newton Group (INT, WHT) in the Spanish Observatorio del Roque de Los Muchachos of the Instituto de Astrofísica de Canarias. Based on observations made at the Centro Astronómico Hispano Alemán (CAHA) at Calar Alto, operated by the Max-Planck Institut für Astronomie and the Instituto de Astrofísica de Andalucía (CSIC).

⋆⋆ Appendices are only available in electronic form at http://www.aanda.org

the interstellar medium (ISM) that eventually will form the next generation of stars. Accurate oxygen abundance measurements of several H II regions within a dwarf galaxy will increase the understanding of its chemical enrichment and mixing of enriched material. The analysis of the kinematics of the ionized gas will also help to understand the dynamic stage of galaxies and reveal recent interaction features. Furthermore, detailed analyses of starburst galaxies in the nearby Universe are fundamental to interpret the observations of high-z star forming galaxies, such as Lyman Break Galaxies (Erb et al. 2003), as well as quantify the importance of interactions in the triggering of the star-formation bursts, which seem to be very common at higher redshifts (i.e., Kauffmann & White 1993; Springel et al. 2005).

The comparison of the metallicity (which reflects the gas reprocessed by stars and any exchange of gas between the galaxy and its environment) with the stellar mass (which reflects the amount of gas locked up into stars) provides key clues about galaxy formation and evolution. These analyses have shown a clear correlation between mass and metallicity. In practice, luminosity has been used as substitute of mass because of the difficulty of deriving reliable galaxy masses, yielding to the so-called metallicity–luminosity relation (i.e., Rubin et al. 1984; Richer & McCall 1995; Salzer et al. 2005), although in recent years mass–metallicity relations are also explored (i.e., Tremonti et al. 2004; Kewley & Elisson 2008), and are studied even at high redshifts (i.e., Kobulnicky et al. 1999; Pettini et al. 2001; Kobulnicky & Kewley 2004; Erb et al. 2006; Liang et al. 2006). The evolution of such relationships are now predicted by semi-analytic models of galaxy formation within the Λ-cold dark matter framework that include chemical hydrodynamic simulations (De Lucia et al. 2004; Tissera et al. 2005; De Rossi et al. 2006; Davé & Oppenheimer 2007). Ironically, today the main problem is not to estimate the mass of a galaxy but its real metallicity, so that different methods involving direct estimates of the oxygen abundance, empirical calibrations using bright emission-line ratios or theoretical methods based on photoionization models yield very different values (i.e., Yin et al. 2007; Kewley & Elisson 2008).

Hence precise photometric and spectroscopic data, including a detailed analysis of each particular galaxy that allows conclusions about its nature, are crucial to address these issues. We performed such a detailed photometric and spectroscopic study in a sample of strong star-forming galaxies, many of them previously classified as dwarf galaxies. The majority of these objects are Wolf-Rayet (WR) galaxies, a very inhomogeneous class of star-forming objects which share at least an ongoing or recent star formation event that has produced stars sufficiently massive to evolve into the WR stage (Schaerer et al. 1999). However, WR features in the spectra of a galaxy provides useful information about the star-formation processes in the system. As the first WR stars typically appear around 2–3 Myr after the starburst is initiated and disappear within some 5 Myr (Meynet & Maeder 2005), their detection gives indications about both the youth and strength of the burst, offering the opportunity to study an approximately coeval sample of very young starbursts (Schaerer & Vacca 1998).

The main aim of our study of the formation of massive stars in starburst galaxies and the role that the interactions with or between dwarf galaxies and/or low surface brightness objects have in its triggering mechanism. In Paper I (López-Sánchez & Esteban 2008) we described the motivation of this work, compiled the list of the 20 analysed WR galaxies (Table 1 of Paper I), the majority of them showing several sub-regions or objects within or surrounding them, and presented the results of the optical/*NIR* broad-band and Hα photometry. In Paper II (López-Sánchez & Esteban 2009) we presented the results of the analysis of the intermediate resolution long-slit spectroscopy of 16 WR galaxies of our sample – the results for the other four galaxies were published separately. In many cases, two or more slit positions were used to analyse the most interesting zones, knots or morphological structures belonging to each galaxy or even surrounding objects. Paper III (López-Sánchez & Esteban 2010) presented the analysis of the O and WR stellar populations within these galaxies. In this paper, the forth of the series, we globally compile and analyse the optical/*NIR* photometric data (Sect. 2) and study the physical (Sect. 3) and chemical (Sect. 4) properties of the ionized gas within our galaxy sample. Thirty-one up to 41 regions have a direct estimate of the electron temperature of the ionized gas, and hence the element abundances were derived with the direct method. Section 4 includes the analysis of the N/O ratio with the oxygen abundance, a discussion of the nitrogen enrichment in WR galaxies, a study of the α-elements to oxygen ratio with the oxygen abundance, and the comparison of the results provided by the most common empirical calibrations with those derived following the direct method (the Appendix compiles all metallicity calibrations used in this work). Section 5 analyses the metallicity–luminosity relations obtained with our data. Section 6 discusses the relations between the metallicity and the optical/*NIR* colours. Finally, we list our main conclusions in Sect. 7.

The final paper of the series (Paper V) will compile the properties derived with data from other wavelengths (UV, FIR, radio, and X-ray) and complete a global analysis of all available multiwavelength data of our WR galaxy sample. We have produced the most comprehensive data set of these galaxies so far, involving multiwavelength results and analysed according to the same procedures.

2. Global analysis of magnitudes and colours

Our optical and *NIR* broad-band photometric results for the galaxy sample were presented in Paper I. These data allowed us the analysis of the optical and *NIR* magnitudes and the colours of the galaxies and surrounding dwarf objects. Table 1 compiles the optical/*NIR* results for the individual galaxies, not considering regions within them or nearby diffuse objects. This table shows the colour excess, $E(B-V)$ (derived with the Balmer decrement in our optical spectra, see Paper II), the absolute B-magnitude (both corrected, M_B, and uncorrected, $M_B^{\rm NC}$, for extinction), all the optical/*NIR* colours, and the age of the most recent star-formation burst (the young population, derived from our Hα images) and the minimum age of the old stellar population (usually estimated from the low luminosity component or regions without nebular emission using our optical/*NIR* broad-band images).

Our first result from Table 1 is that the actual number of dwarf galaxies, defined as $M_B \geq -18$, is not as high as we had expected considering the selection criteria of our WR galaxy sample. There are two reasons for this: (i) on the one hand, the determination of the magnitudes was performed in a more accurate way. As our images are deeper than those previously obtained, the integrated magnitude of a diffuse object is *lower* than that estimated before. (ii) On the other hand, we corrected all our data for extinction, but not only considering the effect of the dust in the Milky Way as it is usually done, but taking into account the internal extinction derived from our spectroscopic data. That is why only six galaxies (Mkn 5, SBS 0926+606, SBS 1054+365, SBS 1211+540, SBS 1415+437 and NGC 5253) are strictly classified as dwarf galaxies following the above definition.

Table 1. Compilation of the broad-band photometric data[a] for the individual galaxies analysed in this work.

Galaxy	$E(B-V)$ (a)	M_B^{NC} (b)	M_B (c)	$U-B$ (d)	$B-V$ (d)	$V-R$ (d)	$V-J$ (d)	$J-H$ (d)	$H-K_s$ d)	B. Age (e)	UC Age (f)
HCG 31 AC	0.06	–19.18	–19.43	–0.60 ± 0.06	0.03 ± 0.08	0.12 ± 0.08	0.20 ± 0.10	0.13 ± 0.10	0.15 ± 0.12	5.0	100
HCG 31 B	0.18	–17.96	–18.71	–0.38 ± 0.08	0.17 ± 0.06	0.06 ± 0.06	0.14 ± 0.10	0.13 ± 0.10	0.12 ± 0.10	7.0	100
HCG 31 E	0.06	–15.51	–15.76	–0.65 ± 0.10	–0.03 ± 0.10	0.20 ± 0.09	0.29 ± 0.12	0.05 ± 0.10	0.18 ± 0.12	6.0	–
HCG 31 F1	0.20	–14.93	–15.76	–0.99 ± 0.12	–0.07 ± 0.12	–0.04 ± 0.10	–0.17 ± 0.14	0.04 ± 0.17	0.29 ± 0.30	2.5	0
HCG 31 F2	0.09	–13.97	–14.34	–1.01 ± 0.12	–0.09 ± 0.12	–0.02 ± 0.10	0.01 ± 0.16	0.08 ± 0.30	0.20 ± 0.50	2.5	0
HCG 31 G	0.06	–18.63	–18.88	–0.43 ± 0.09	–0.01 ± 0.08	0.14 ± 0.08	0.45 ± 0.08	0.12 ± 0.10	0.13 ± 0.10	6.0	100
Mkn 1087	0.17	–21.45	–22.15	–0.41 ± 0.08	0.17 ± 0.08	0.20 ± 0.08	0.52 ± 0.06	0.20 ± 0.06	0.16 ± 0.06	6.0	100
Mkn 1087 N	0.10	–17.65	–18.06	...	–0.05 ± 0.06	0.14 ± 0.10	0.21 ± 0.08	0.18 ± 0.08	0.13 ± 0.08	7.0	–
Mkn 1087 #1	0.07[g]	-16.05	-16.34	–0.75 ± 0.15	–0.01 ± 0.10	0.10 ± 0.08	...	...	...	6.0	–
Mkn 1087 #3	0.07[g]	–16.91	–17.20	0.08 ± 0.30	0.11 ± 0.06	0.26 ± 0.06	0.64 ± 0.10	0.50 ± 0.20	...	–	150
Haro 15	0.11	–20.41	–20.87	–0.52 ± 0.08	0.26 ± 0.08	0.32 ± 0.08	0.17 ± 0.08	0.58 ± 0.08	0.22 ± 0.08	5.0	500
Mkn 1199	0.15	–20.06	–20.68	–0.44 ± 0.06	0.46 ± 0.06	0.29 ± 0.06	1.30 ± 0.07	0.55 ± 0.08	0.34 ± 0.08	8.0	500
Mkn 1199 NE	0.11	–17.11	–17.57	0.16 ± 0.08	0.51 ± 0.08	0.34 ± 0.08	1.29 ± 0.08	0.62 ± 0.10	0.20 ± 0.10	12.0	500
Mkn 5	0.20	–14.74	–15.57	–0.41 ± 0.06	0.44 ± 0.06	0.30 ± 0.06	0.81:	0.52 ± 0.03	0.38 ± 0.04	5.0	500
IRAS 08208+2816	0.17	–20.59	–21.29	–0.49 ± 0.06	0.22 ± 0.06	0.35 ± 0.08	1.03 ± 0.08	0.54 ± 0.08	0.22 ± 0.10	5.5	500
IRAS 08339+6517	0.16	–20.91	–21.57	–0.51 ± 0.08	0.01 ± 0.08	0.26 ± 0.08	1.36 ± 0.06	0.64 ± 0.05	0.23 ± 0.06	4.5	150
IRAS 08339+6517 C	0.13	–17.67	–18.21	–0.16 ± 0.10	0.20 ± 0.08	0.26 ± 0.08	1.45 ± 0.12	0.21 ± 0.25	0.68 ± 0.28	5.5	250
POX 4	0.06	–18.54	–18.79	–0.68 ± 0.03	0.29 ± 0.02	0.32 ± 0.04	0.42 ± 0.08	0.28 ± 0.08	0.15 ± 0.10	3.5	250
POX 4 Comp	0.12	–14.86	–15.36	–0.02 ± 0.06	0.25 ± 0.02	0.30 ± 0.04	0.87 ± 0.10	0.7:	0.3:	5.0	300
UM 420	0.06	–19.30	–19.55	–0.80 ± 0.06	0.31 ± 0.06	0.13 ± 0.06	0.77 ± 0.12	0.41 ± 0.12	0.12 ± 0.16	4.5	200
SBS 0926+606 A	0.08	–16.96	–17.29	–0.75 ± 0.06	0.01 ± 0.06	0.14 ± 0.06	0.54 ± 0.06	0.21 ± 0.06	0.15 ± 0.08	4.8	200
SBS 0926+606 B	0.12	–16.87	–17.37	–0.51 ± 0.08	0.08 ± 0.06	0.20 ± 0.06	0.83 ± 0.06	0.29 ± 0.06	0.18 ± 0.08	6.7	100
SBS 0948+532	0.24	–17.44	–18.43	–1.20 ± 0.06	–0.12 ± 0.06	0.16 ± 0.06	...	...	...	4.6	100
SBS 1054+365	0.02	–13.98	–14.06	–0.34 ± 0.06	0.33 ± 0.06	...	0.92 ± 0.08	0.38 ± 0.12	0.16 ± 0.15	4.9	500
SBS 1211+540	0.08	–12.94	–13.27	–0.61 ± 0.06	0.04 ± 0.06	0.21 ± 0.06	...	...	...	4.7	500
SBS 1319+579	0.02	–18.45	–18.53	–0.39 ± 0.06	0.34 ± 0.06	0.19 ± 0.06	1.03 ± 0.08	0.39 ± 0.12	0.16 ± 0.20	3.7	300
SBS 1415+437	0.13	–14.09	–14.52	–0.47 ± 0.06	0.21 ± 0.06	0.27 ± 0.06	0.98 ± 0.08	0.35 ± 0.10	0.15:	3.6	250
III Zw 107	0.21	–19.27	–20.14	–0.42 ± 0.06	0.14 ± 0.06	0.22 ± 0.06	0.62 ± 0.12	0.47 ± 0.20	0.35±0.20	5.6	500
Tol 9	0.31	–17.98	–19.26	–0.34 ± 0.06	0.24 ± 0.06	0.22 ± 0.06	0.83 ± 0.08	0.68 ± 0.10	0.27 ± 0.12	5.8	500
Tol 1457-262 Obj1	0.16	–19.07	–19.73	–0.56 ± 0.06	0.23 ± 0.06	0.26 ± 0.06	0.60 ± 0.10	0.51 ± 0.12	0.22 ± 0.12	4.6	500
Tol 1457-262 Obj2	0.16[g]	–18.31	–18.97	–0.42 ± 0.06	0.34 ± 0.06	0.36 ± 0.06	0.90 ± 0.10	0.58 ± 0.12	0.27 ± 0.14	5.2	500
Tol 1457-262 #15	0.16[g]	–15.82	–16.48	–0.25 ± 0.10	0.39 ± 0.08	0.39 ± 0.06	1.10 ± 0.20	...	...	6.4	400
Tol 1457-262 #16	0.16[g]	–14.03	–14.69	–0.10 ± 0.15	0.45 ± 0.10	0.40 ± 0.06	...	...	...	7.0	500
ESO 566-8	0.34	–19.47	–20.88	–0.48 ± 0.06	0.31 ± 0.06	0.19 ± 0.06	1.10 ± 0.10	0.60 ± 0.12	0.38 ± 0.14	4.2	500
ESO 566-7	0.16	–18.69	–19.35	–0.21 ± 0.08	0.49 ± 0.06	0.31 ± 0.06	1.20 ± 0.10	0.71 ± 0.16	0.34 ± 0.16	4.2	500
NGC 5253[h]	0.17	–17.23	–17.92	–0.41 ± 0.02	0.27 ± 0.02	0.21 ± 0.02	0.81 ± 0.03	0.53 ± 0.04	0.19 ± 0.05	3.5	300

Notes. [a] Colour excess, $E(B-V)$, derived from our estimates of the reddening coefficient and assuming $R_V = 3.1$, $E(B-V) = 0.692c(\mathrm{H}\beta)$. [b] Absolute B-magnitude, not corrected for extinction. [c] Extinction-corrected absolute B-magnitude, assuming $M_B = M_B^{\mathrm{NC}} - A_B = M_B^{\mathrm{NC}} - 3.1 \times 1.337E(B-V) = M_B^{\mathrm{NC}} - 2.868\ c(\mathrm{H}\beta)$. [d] All colours have been corrected for both extinction and emission of the gas, see López-Sánchez, Esteban (2008). [e] Age of the most recent star-forming burst (derived using the Hα equivalent width), in Myr. [f] Minimum age of the underlying stellar population (derived via the analysis of the low-luminosity component of the galaxy), in Myr. [g] $E(B-V)$ was estimated only considering the extinction of the Milky Way. [h] Optical and *NIR* magnitudes extracted from the NED and corrected for extinction using an average value of $c(\mathrm{H}\beta)$= 0.24, see López-Sánchez et al. (2007) .

POX 4, SBS 0948+532 and SBS 1319+579 could be also considered dwarf galaxies because $M_B \geq -19$. Table 1 also lists some tidal dwarf galaxy (TDG) candidates (HCG 31 E, F1 and F2; Mkn 1087 #1 and #3, POX 4 Comp) and nearby external objects (Mkn 1087 N, Mkn 1199 NE, IRAS 08309+6517 C, Tol 1457-262 #15 and #16) surrounding a main galaxy. However, as we remarked in Paper I and in the analysis of the HCG 31 members (López-Sánchez et al. 2004a), we must keep in mind that the B-magnitude of a starburst is increased by several magnitudes during the first 10 Myr with respect to its brightness in the quiescent phase, so we should expect that some of the objects with $-18 \geq M_B \geq -19.5$ are indeed defined as dwarf objects during their quiescent phase.

In order to quantify the effect of the correction for extinction, we plot the uncorrected absolute B-magnitude versus the absolute B-magnitude corrected for extinction in Fig. 1. We did not consider the correction for the emission of the gas in the absolute magnitude because (i) it is small in the B-filter, less than 0.10 magnitudes and, more important; (ii) we are considering the magnitude of the galaxy as a whole, taking into account both the star-forming bursts and regions dominated by older stellar populations that *do not* possess any nebular emission. From Fig. 1, we see that the magnitudes corrected for extinction are on average around 0.60 magnitudes lower than when this effect is not considered. As all data lie in a narrow band, we performed a linear fit, finding the following relation between both magnitudes:

$$M_B = 1.02M_B^{\mathrm{nc}} - 0.19. \quad (1)$$

For $M_B = -18$, the magnitude difference is $\Delta M_B \sim 0.56$. Transforming this value to luminosity, the consideration of the correction for extinction means that one has to multiply the observed B-luminosity of a galaxy by a factor between 1.6 (for

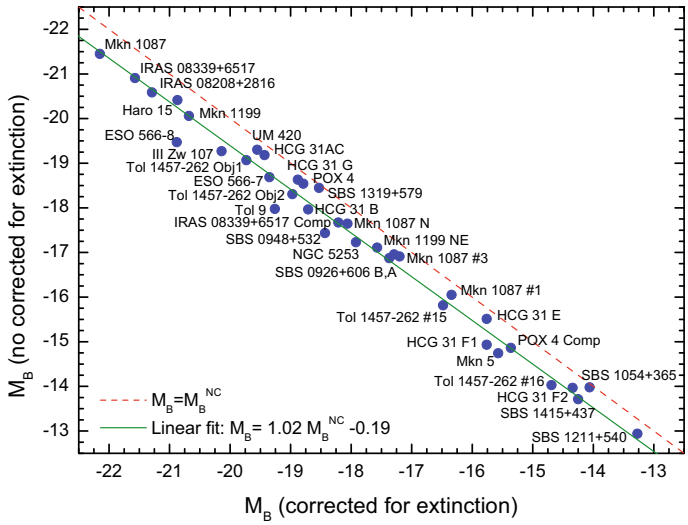

Fig. 1. Comparison between the reddening-corrected absolute B-magnitudes (M_B) and the uncorrected ones (M_B^{NC}) for all individual galaxies analysed in this work. A linear fit to the data is shown.

$M_B \sim -16$) and 1.8 (for $M_B \sim -22$). We note that there is a slight dependence on the extinction with the absolute magnitude of the galaxy, that is, the correction for extinction is higher at lower absolute magnitudes. This suggests a higher absorption of the light in brighter systems (more amount of dust). We will get the same result when we analyse the relation between the reddening coefficient and the warm dust mass (Paper V).

As we explained in Paper I, we compared our optical/NIR colours (corrected for extinction and emission of the ionized gas) with the predictions given by three different population synthesis models, STARBURST99 (Leitherer et al. 1999), PEGASE.2 (Fioc & Rocca-Volmerange 1997) and Bruzual & Charlot (2003), to estimate the age of the dominant stellar population of the galaxies, the star-forming regions, and the underlying stellar component. We assumed an instantaneous burst with a Salpeter IMF a total mass of 10^6 $M_\odot$, and a metallicity of $Z/Z_\odot$= 0.2, 0.4 and 1 (chosen as a function of the oxygen abundance of the galaxy derived from our spectroscopic data, see Paper II) for all models.

We found a relatively good correspondence (see Figs. 37–39, top, in Paper I) between the optical/*NIR* data and the models, especially for compact and dwarf objects such as HCG 31 F1 or SBS 0948+532, the ages being consistent with a recent star-formation event (≤100 Myr). We remark here

1. the quality of the observational data and the data reduction process, which was performed in detail and in an homogeneous way for all galaxies,
2. the we corrected the data for extinction and reddening, considering the $c(\mathrm{H}\beta)$ value derived from the spectroscopic data obtained for each region (Paper II). As we have seen, this correction is important and very often it is not performed in the analysis of the colours of extragalactic objects, which only consider the extinction of the Milky Way in the direction to the analysed galaxy,
3. and the correction of the colours for the gas emission using our spectroscopic data. This effect is not important in some galaxies, but it seems fundamental when analysing compact objects with strong nebular emission, such as BCDGs or regions within a galaxy possessing an strong starburst.

Some discordances between the colours and the predictions of the theoretical models (∼0.2 mag or even higher) are always found in galaxies hosting a considerable population of old stars (Mkn 1199, Mkn 5, Tol 1457-262 #15 and #16, ESO 566-7), because their luminosities barely contribute to the U magnitude. Hence, the young stellar population usually dominates the $U-B$ colour, but the rest of the colours ($B-V$, $V-R$, $V-J$, $H-K_s$) posses an important contribution of the old stellar population. If the bursts and the underlying stellar population are analysed independently, the agreement between colours and the predictions given by the models is closer that when considering the galaxies as a whole. The last columns in Table 1 compile the ages estimated for the most recent star-forming event and the underlying population component (if possible) for all individual galaxies derived from optical/*NIR* colours. Because the theoretical models are optimized to study the youngest stellar populations within the galaxies, in some cases we considered a lower limit of 500 Myr for the age of the underlying component (UC).

Figure 2 shows several colour–colour diagrams comparing the predictions given by evolutionary synthesis models with the colours (corrected for both reddening and contribution of the emission lines) of our galaxy sample when the burst (blue stars) and underlying component (UC, red squares) of each system are considered independently. The correspondence has improved now. Indeed, all inferred ages of the most recent star-formation burst are lower than 25 Myr, while the data corresponding to the underlying component suggest ages higher than 100 Myr. Therefore, a proper estimate of the stellar population age for this type of galaxy using broad-band filters is only obtained when bursts and underlying components are independently considered.

There are still some discrepancies that can be explained by a lack of good separation between regions with and without star-formation activity. The comparison of the $V-R$ colour vs. the $U-B$ colour in data of the UC also suggest that in some galaxies the old stellar population colours are not explained by just one single-age population, but at least two of them are needed (i.e., for SBS 1415+437, the UC colour may be explained by a mix of two stellar populations with ages of ∼150 Myr and ≥500 Myr, see Sect. 3.15.1 in Paper I). However, the best method to analyse the colours and luminosities of the host component in starburst systems (specially, in BCGs) is performing a careful 2D analysis of their structural parameters (i.e. Amorín et al. 2007, 2009). Some of the galaxies analysed by these authors were also studied here. Their results of the colours of the UC (the host) agree well within the errors with those estimated here, for example, for Mkn 5 they compute $(B-V)_{\mathrm{UC}} = 0.40 \pm 0.28$ and $(V-R)_{\mathrm{UC}} = 0.28 \pm 0.16$, while in this work we derived $(B-V)_{\mathrm{UC}} = 0.45 \pm 0.08$ and $(V-R)_{\mathrm{UC}} = 0.30 \pm 0.08$ for the same object.

Figure 3 plots the Hα equivalent width (obtained from our narrow-band images) as a function of the $U-B$ colour (obtained from our broad-band images) for the bursts within the analysed galaxies. We remark that the $W(\mathrm{H}\alpha)$ derived from the Hα images agree quite well with those obtained from the optical spectroscopy (see Paper II). This figure compares the observational data with some STARBURST 99 models (Leitherer et al. 1999) at different metallicities. As we see, the agreement is quite good for almost all objects. This also indicates both the quality of our data and the success of the theoretical models to reproduce the young star-forming populations.

However, if we compare the $W(\mathrm{H}\alpha)$ and the $U-B$ colour considering the total extension of each galaxy (and not only the burst component), this agreement is less good. In this case, data

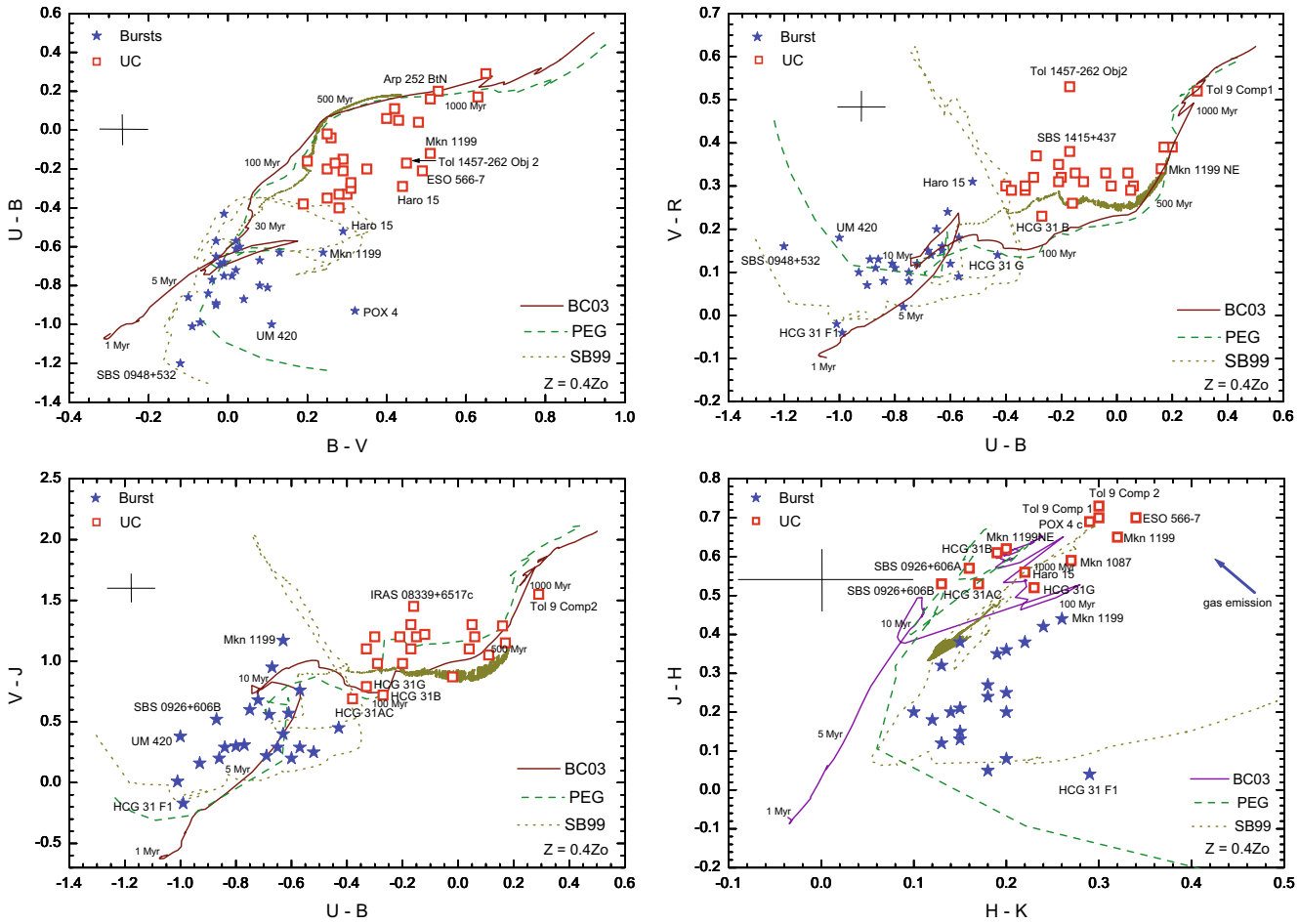

Fig. 2. Colour–colour diagrams comparing the predictions given by evolutionary synthesis models (continous line: BC03, Bruzual & Charlot 2003, models; discontinuous line: PEGASE.2, Fioc & Rocca-Volmerange 1997, models; dotted line: STARBURST 99, Leitherer et al. 1999, assuming $Z = 0.4Z_{\odot}$) with the colours (corrected for both reddening and contribution of the emission lines) of our galaxy sample when the burst (blue stars) and underlying component (UC, red squares) of each system are considered independently. The cross indicates the typical errors in our data. Some age labels were included for the BC03 models.

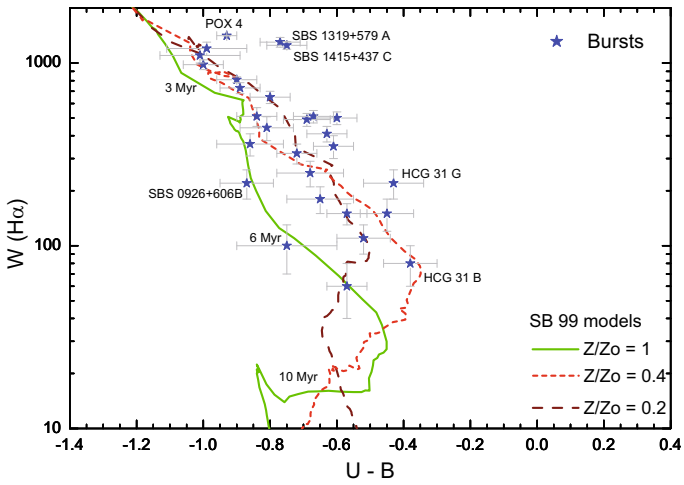

Fig. 3. $W(\mathrm{H}\alpha)$ vs. $U-B$ diagram comparing the predictions of the theoretical models of STARBURST 99 (Leitherer et al. 1999) for three different metallicities with the data corresponding to the star-forming bursts analysed in our sample galaxy.

with a fixed $W(\mathrm{H}\alpha)$ have a redder $U-B$ colour than that predicted by the models. This is explained because the $U-B$ colour is slightly contaminated with the light of older stellar populations or regions with no nebular emission. Hence, as we emphasized before, it is important to distinguish between the pure starburst regions and the underlying component to get a good estimate of the properties of these galaxies and, in particular, the strong star-forming regions.

The age of the last starburst event experienced by each galaxy and the minimum age of its old stellar populations are compiled in the last two columns of Table 1. Except for a few objects (HCG 31 members E, F1 and F2 and Mkn 1087 members N and #1) for which it was not possible to estimate the colours of the UC, all analysed galaxies show an older stellar population underlying the bursts. Indeed, in many cases the colours of the UC suggest ages older than 500 Myr. This clearly indicates that all galaxies have experienced a previous star-formation events long time before those they are now hosting, as concluded in many other previous results (i.e. Cairós et al. 2001a,b; Bergvall & Östlin 2002; Papaderos et al. 2006; Amorín et al. 2009). However, as we previously said (López-Sánchez et al. 2004a), this seems not to be true in the particular case of members F of HCG 31, which clearly show no evidences of underlying old stellar populations. This was recently confirmed by deep *Hubble Space Telescope* imaging (Gallagher et al. 2010), and hence these two objects are very likely experiencing their very first star-formation event.

Table 2. Physical properties of the ionized gas for the galaxies analysed in this work.

Galaxy	T_e [(a)]	T_e High [K]	T_e Low [K]	n_e [cm^{-3}]	$c(H\beta)$	W_{abs} [Å]	$-W(H\beta)$ [Å]
HCG 31 AC	D	9400 ± 600	10 800 ± 300	210 ± 70	0.09 ± 0.03	2.0	91.1 ± 2.1
HCG 31 B	D	11 500 ± 700	12 000 ± 400	<100	0.28 ± 0.08	2.0	12.9 ± 0.5
HCG 31 E	D	11 100 ± 1000	11 800 ± 600	<100	0.11 ± 0.05	2.0	21.1 ± 1.1
HCG 31 F1	D	12 600 ± 1100	12 600 ± 700	<100	0.32 ± 0.06	2.0	218 ± 13
HCG 31 F2	D	12 300 ± 1300	12 400 ± 800	<100	0.14 ± 0.05	2.0	256 ± 30
HCG 31 G	D	11 600 ± 700	12 000 ± 400	<100	0.09 ± 0.05	2.0	37.0 ± 1.6
Mkn 1087	EC	7100 ± 1000	8000 ± 1000	220 ± 50	0.17 ± 0.02	1.7 ± 0.2	22.3 ± 0.9
Mkn 1087 N	EC	10 900 ± 1000	10 600 ± 1000	115 ± 50	0.17 ± 0.02	0.2 ± 0.1	25.0 ± 1.7
Haro 15 C	EC	9500 ± 800	9600 ± 600	<100	0.11 ± 0.03	2.4 ± 0.4	16.4 ± 1.1
Haro 15 A	D	12 850 ± 700	12 000 ± 500	<100	0.33 ± 0.03	1.3 ± 0.3	75.7 ± 4.2
Mkn 1199	D	5400 ± 700	6800 ± 600	300 ± 100	0.30 ± 0.03	1.8 ± 0.4	21.4 ± 1.3
Mkn 1199 NE	EC	8450 ± 800	8900 ± 600	<100	0.16 ± 0.03	0.6 ± 0.3	20.2 ± 2.3
Mkn 5	D	12 450 ± 650	11 700 ± 450	<100	0.17 ± 0.02	0.8 ± 0.2	75 ± 5
IRAS 08208+2816	D	10 100 ± 700	10 100 ± 500	<100	0.11 ± 0.02	3.2 ± 0.1	80 ± 5
IRAS 08339+6517	EC	8700 ± 1000	9100 ± 1000	100	0.22 ± 0.02	1.8 ± 0.2	19.0 ± 0.8
IRAS 08339+6517c	EC	9 050 ± 1000	9300 ± 1000	100	0.18 ± 0.03	1.5 ± 0.2	7.5 ± 0.2
POX 4	D	14 000 ± 500	12 800 ± 400	250 ± 80	0.08 ± 0.01	2.0 ± 0.1	200 ± 9
POX 4 Comp	EC	12 400 ± 1000	11 700 ± 700	<100	0.06 ± 0.03	1.4 ± 0.3	12 ± 4
UM 420	D	13 200 ± 600	12 200 ± 500	140 ± 80	0.09 ± 0.01	2.0 ± 0.1	169 ± 10
SBS 0926+606 A	D	13 600 ± 700	12 500 ± 500	<100	0.12 ± 0.03	0.7 ± 0.1	125 ± 6
SBS 0926+606 B	EC	11 500 ± 1000	11 000 ± 800	<100	0.18 ± 0.04	1.0 ± 0.3	18 ± 3
SBS 0948+532	D	13 100 ± 600	12 200 ± 400	250 ± 80	0.35 ± 0.03	0.3 ± 0.1	213 ± 11
SBS 1054+365	D	13 700 ± 900	12 600 ± 700	<100	0.02 ± 0.02	0.8 ± 0.1	89 ± 7
SBS 1054+365 b	EC	11 800 ± 1100	11 300 ± 900	300 ± 200	0.03 ± 0.03	0.3 ± 0.1	8 ± 3
SBS 1211+540	D	17 100 ± 600	15 000 ± 400	320 ± 50	0.12 ± 0.01	1.3 ± 0.1	135 ± 10
SBS 1319+579 A	D	13 400 ± 500	12 400 ± 400	<100	0.03 ± 0.01	0.0 ± 0.1	285 ± 14
SBS 1319+579 B	D	11 900 ± 800	11 300 ± 600	<100	0.11 ± 0.03	0.4 ± 0.1	42 ± 4
SBS 1319+579 C	D	11 500 ± 600	11 050 ± 400	<100	0.02 ± 0.02	0.2 ± 0.1	94 ± 6
SBS 1415+579 C	D	16 400 ± 600	14 500 ± 400	<100	0.01 ± 0.02	0.8 ± 0.1	222 ± 11
SBS 1415+579 A	D	15 500 ± 700	13 850 ± 500	<100	0.15 ± 0.03	1.0 ± 0.2	130 ± 8
III Zw 107 A	D	10 900 ± 900	10 500 ± 800	200 ± 60	0.68 ± 0.04	2.0 ± 0.3	44 ± 2
Tol 9	D	7600 ± 1000	8300 ± 700	180 ± 60	0.50 ± 0.05	7.5 ± 0.8	33 ± 2
Tol 1457-262 A	D	14 000 ± 700	12 500 ± 600	200 ± 80	0.57 ± 0.03	1.4 ± 0.2	101 ± 6
Tol 1457-262 B	D	15 200 ± 900	14 200 ± 700	<100	0.00 ± 0.05	0.0 ± 0.1	82 ± 7
Tol 1457-262 C	D	13 400 ± 1100	12 400 ± 1000	200 ± 100	0.15 ± 0.02	0.7 ± 0.1	92 ± 9
ESO 566-8	D	8700 ± 900	9100 ± 800	300 ± 100	0.49 ± 0.03	1.3 ± 0.1	95 ± 7
ESO 566-7	EC	7900 ± 1000	8500 ± 900	100 ± 50	0.23 ± 0.05	2.7 ± 0.2	13 ± 2
NGC 5253 A	D	12 100 ± 260	11 170 ± 520	580 ± 110	0.23 ± 0.02	1.3 ± 0.1	234 ± 5
NGC 5253 B	D	12 030 ± 260	11 250 ± 490	610 ± 100	0.38 ± 0.03	1.7 ± 0.1	254 ± 5
NGC 5253 C	D	10 810 ± 230	10 530 ± 470	370 ± 80	0.25 ± 0.03	0.8 ± 0.1	94 ± 3
NGC 5253 D	D	11 160 ± 510	10 350 ± 650	230 ± 70	0.10 ± 0.02	0.6 ± 0.1	39 ± 2

Notes. [(a)] In this column we indicate if T_e was computed using the direct method (D) or via empirical calibrations (EC).

3. Physical properties of the ionized gas

Table 2 compiles all the high- and low-ionization electron temperatures of the ionized gas, T_e, electron density n_e, reddenning coefficient $c(H\beta)$, equivalent width of the underlying stellar absorption in the Balmer H I lines W_{abs}, and the Hβ equivalent width, for the galaxies analysed in this work (see Paper II). Thirty-one up to 41 of the objects listed in Table 2 have a direct estimate of the electron temperature of the ionized gas. For most, this was computed using the [O III] ratio involving the nebular [O III] $\lambda\lambda$4959,5007 and the auroral [O III] λ4363 emission lines. In most objects, the low-ionization electron temperature was not computed directly but assuming the relation between T_e(O III) and T_e(O II) provided by Garnett (1992). Half of the objects of our galaxy sample (22) have electron densities lower than 100 cm^{-3}.

We explored possible correlations among some of the different quantities compiled in Table 2 as well as the oxygen abundance (see Table 3) computed for the objects. First, we checked the nature of the ionized gas of the sample galaxies. Figure 4 plots the typical diagnostic diagrams between bright emission lines and the predictions given by the photoionized models provided by Dopita et al. (2000) for extragalactic H II regions (that assume instantaneous star-formation within star-forming regions) and the Kewley et al. (2001) models for starburst galaxies (which consider continuous star formation and more realistic assumptions about the physics of starburst galaxies).

Table 3. Chemical properties of the ionized gas for the galaxies analysed in this work.

Galaxy	T_e[a]	12+log(O/H)	log $\frac{O^{++}}{O^+}$	log(N/O)	log(S/O)	log(Ne/O)	log(Ar/O)	log(Fe/O)
HCG 31 AC	D	8.22 ± 0.05	1.51 ± 0.12	−1.12 ± 0.08	...	−0.93 ± 0.12	...	−2.12 ± 0.21
HCG 31 B	D	8.14 ± 0.08	0.63 ± 0.09	−1.39 ± 0.10	−1.67 ± 0.14	−0.42 ± 0.13	...	−1.87 ± 0.32
HCG 31 E	D	8.13 ± 0.09	1.00 ± 0.11	−1.26 ± 0.12	−1.58 ± 0.15	−0.42 ± 0.14	...	−1.77 ± 0.32
HCG 31 F1	D	8.07 ± 0.06	3.72 ± 0.32	−1.27 ± 0.11	−1.69 ± 0.15	−0.80 ± 0.17	...	–1.9:
HCG 31 F2	D	8.03 ± 0.10	2.19 ± 0.21	−1.43 ± 0.16	−1.67 ± 0.18	−0.76 ± 0.20	...	...
HCG 31 G	D	8.15 ± 0.07	1.15 ± 0.11	−1.31 ± 0.10	−1.67 ± 0.22	−0.56 ± 0.14	...	–2.0:
Mkn 1087	EC	8.57 ± 0.10	0.55 ± 0.18	−0.81 ± 0.12	−1.78 ± 0.16	−0.45 ± 0.17	...	...
Mkn 1087 N	EC	8.23 ± 0.10	0.99 ± 0.25	−1.46 ± 0.15	...	−0.52 ± 0.19	...	...
Haro 15 C	EC	8.37 ± 0.10	−0.23 ± 0.16	−1.03 ± 0.15	−1.71 ± 0.18	−0.65 ± 0.18	...	–2.2:
Haro 15 A	D	8.10 ± 0.06	0.66 ± 0.10	−1.35 ± 0.11	−1.89 ± 0.15	−0.68 ± 0.12	...	–1.6:
Mkn 1199	D	8.75 ± 0.12	−0.36 ± 0.16	−0.62 ± 0.10	−1.54 ± 0.14	−0.58 ± 0.17	...	−1.86 ± 0.26
Mkn 1199 NE	EC	8.46 ± 0.13	−0.19 ± 0.09	−1.20 ± 0.11	−1.54 ± 0.17	−0.65 ± 0.18	...	...
Mkn 5	D	8.07 ± 0.04	0.25 ± 0.08	−1.38 ± 0.07	−1.62 ± 0.11	−0.80 ± 0.13	−2.31 ± 0.12	−1.96 ± 0.18
IRAS 08208+2816	D	8.33 ± 0.08	0.43 ± 0.12	−0.89 ± 0.11	−1.64 ± 0.16	−0.67 ± 0.13	−2.51 ± 0.15	−1.95 ± 0.17
IRAS 08339+6517	EC	8.45 ± 0.10	0.53 ± 0.16	−0.94 ± 0.14	...	−0.45 ± 0.18	...	...
IRAS 08339+6517c	EC	8.38 ± 0.10	0.81 ± 0.21	−1.13 ± 0.17	...	–0.55:	...	...
POX 4	D	8.03 ± 0.04	0.74 ± 0.06	−1.54 ± 0.06	−1.80 ± 0.10	−0.78 ± 0.10	...	−2.17 ± 0.11
POX 4c	EC	8.03 ± 0.14	−0.30 ± 0.22	−1.60 ± 0.20	...	-0.60:	...	...
UM 420	D	7.95 ± 0.05	0.00 ± 0.08	−1.11 ± 0.07	−1.66 ± 0.13	−0.71 ± 0.13	...	−2.16 ± 0.13
SBS 0926+606 A	D	7.94 ± 0.08	0.42 ± 0.12	−1.45 ± 0.09	−1.60 ± 0.13	...	−2.34 ± 0.13	−1.99 ± 0.16
SBS 0926+606 B	EC	8.15 ± 0.16	0.21 ± 0.14	−1.35 ± 0.12	...	...	...	...
SBS 0948+532	D	8.03 ± 0.05	0.61 ± 0.08	−1.42 ± 0.08	−1.69 ± 0.14	−0.73 ± 0.12	...	−1.78 ± 0.10
SBS 1054+365	D	8.00 ± 0.07	0.70 ± 0.11	−1.41 ± 0.08	−1.79 ± 0.15	−0.67 ± 0.11	−2.29 ± 0.14	...
SBS 1054+365 b	EC	8.13 ± 0.16	−0.35 ± 0.20	−1.47 ± 0.20	...	...	...	...
SBS 1211+540	D	7.65 ± 0.04	0.69 ± 0.07	−1.62 ± 0.10	−1.47 ± 0.14	−0.75 ± 0.10	...	...
SBS 1319+579 A	D	8.05 ± 0.06	0.77 ± 0.12	−1.53 ± 0.10	−1.76 ± 0.10	...	−2.41 ± 0.11	...
SBS 1319+579 B	D	8.12 ± 0.10	0.16 ± 0.19	−1.49 ± 0.12	−1.76 ± 0.14	...	...	...
SBS 1319+579 C	D	8.15 ± 0.07	0.18 ± 0.13	−1.38 ± 0.10	−1.60 ± 0.11	...	...	–2.3:
SBS 1415+437 C	D	7.58 ± 0.05	0.35 ± 0.08	−1.57 ± 0.08	−1.62 ± 0.12	...	−2.31 ± 0.13	−1.91 ± 0.13
SBS 1415+437 A	D	7.61 ± 0.06	0.42 ± 0.14	−1.57 ± 0.09	−1.72 ± 0.14	...	...	–1.9:
III Zw 107 A	D	8.23 ± 0.09	0.12 ± 0.14	−1.16 ± 0.10	−1.82 ± 0.15	−0.73 ± 0.15	−2.46 ± 0.13	–2.3:
Tol 9	D	8.57 ± 0.10	0.16 ± 0.17	−0.81 ± 0.11	−1.62 ± 0.12	−0.72 ± 0.14	−2.55 ± 0.15	–2.1:
Tol 1457-262 A	D	8.05 ± 0.07	0.27 ± 0.11	−1.57 ± 0.11	−1.88 ± 0.13	−0.88 ± 0.18	−2.50 ± 0.13	–2.2:
Tol 1457-262 B	D	7.88 ± 0.07	0.43 ± 0.11	−1.61 ± 0.12	−1.72 ± 0.18	−0.88 ± 0.20	−2.44 ± 0.18	−1.90 ± 0.22
Tol 1457-262 C	D	8.06 ± 0.11	0.14 ± 0.16	−1.59 ± 0.16	...	−0.84 ± 0.22	−2.45 ± 0.20	...
ESO 566-8	D	8.46 ± 0.11	−0.19 ± 0.17	−0.76 ± 0.12	...	−0.56 ± 0.19	−2.17 ± 0.19	–2.5:
ESO 566-7	EC	8.50 ± 0.16	−0.57 ± 0.22	−0.82 ± 0.16	...	...	−2.49 ± 0.25	...
NGC 5253 A	D	8.18 ± 0.04	2.88 ± 0.18	−0.91 ± 0.07	−1.58 ± 0.08	−0.71 ± 0.08	−2.19 ± 0.07	−2.10 ± 0.12
NGC 5253 B	D	8.19 ± 0.04	3.09 ± 0.14	−1.02 ± 0.07	−1.60 ± 0.08	−0.70 ± 0.08	−2.21 ± 0.07	−2.18 ± 0.11
NGC 5253 C	D	8.28 ± 0.04	1.95 ± 0.13	−1.50 ± 0.08	−1.69 ± 0.09	−0.74 ± 0.08	−2.30 ± 0.08	−2.46 ± 0.14
NGC 5253 D	D	8.31 ± 0.07	0.56 ± 0.14	−1.49 ± 0.10	−1.74 ± 0.13	−0.70 ± 0.15	−2.30 ± 0.13	−2.25 ± 0.16

Notes. [(a)] In this column we indicate if T_e was computed using the direct method (D) or via empirical calibrations (EC).

The dividing line given by the Kewley et al. (2001) models represents an upper envelope of positions of star-forming galaxies. As we see, in all cases the data are found below the theoretical prediction given by this line. This indicates that photoionization is the main excitation mechanism of the gas. We will get the same result when we compare the relation between the *FIR* and the radio-continuum luminosities (Paper V). It is interesting to notice that the observational points included in the diagnostic diagram involving the [O III]/Hβ and [N II]/Hα ratios are located close to the prediction given by the Dopita et al. (2000) models, while points included in the diagnostic diagram that considers the [O III]/Hβ and [S II]/Hα ratios are found very close to the upper envelope given by Kewley et al. (2001). The left panel in Fig. 4 includes the empirical relation between the [O III]/Hβ and the [N II]/Hα ratios provided by Kauffmann et al. (2003) analysing a large data sample of star-forming galaxies from the Sloan Digital Sky Survey (SDSS; York et al. 2000). As can be seen, the comparison of the Kauffmann et al. (2003) relation with our data points also indicates that our objects are experiencing a pure star-formation event, despite a clear offset between both datasets.

W(Hβ) is a good indicator for the age of the most recent star-formation event. The hydrogen ionizing flux of a star cluster gradually decreases as the most massive stars disappear with time, and hence the width of Hβ decreases with time (see Papers I, II and III). Figure 5 plots the relation between the high ionization electron temperature and the Hβ equivalent width. As we see, $|W(\mathrm{H}\beta)|$ increases with increasing T_e, but we must remember that there is a strong correlation between the electron temperature and the oxygen abundance, as high-metallicity H II regions cool more efficiently than low-metallicity H II regions. To study this effect, we used colours to plot four metallicity ranges in Fig. 5. These colours indicate the oxygen abundance range of each object: <7.90, 7.90–8.15, 8.15–8.40 and >8.40, in units of 12 + log(O/H). Although now it is not so evident, it still seems that regions with larger $|W(\mathrm{H}\beta)|$ tend to have higher T_e.

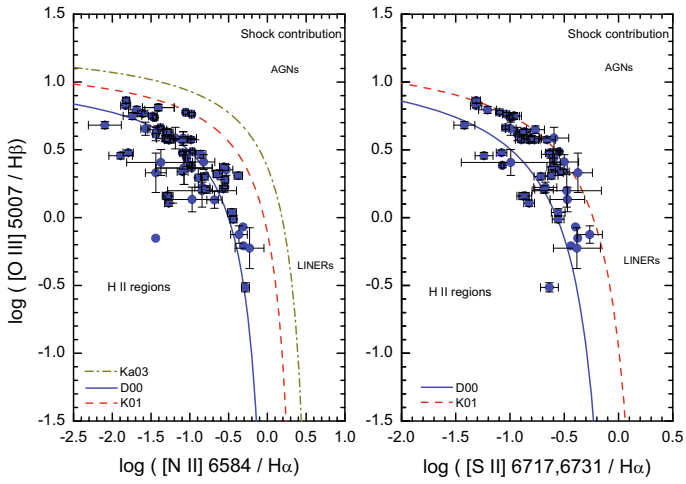

Fig. 4. Comparison of some observational flux ratios obtained for all available regions analysed in this work with the diagnostic diagrams proposed by Dopita et al. (2000), blue continuous line (D00), and Kewley et al. (2001), red discontinuous line (K01). The *left panel* also shows the empirical relation provided by Kauffmann et al. (2003) with a dotted-dashed dark yellow line (Ka03).

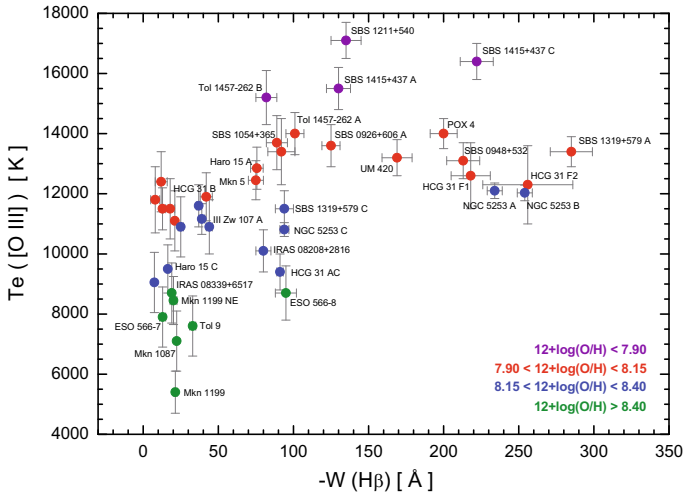

Fig. 5. High ionization electron temperature, T_e(O III), vs. the Hβ equivalent width. The colour-dots indicate the oxygen abundance range of each object. Some objects have been labeled.

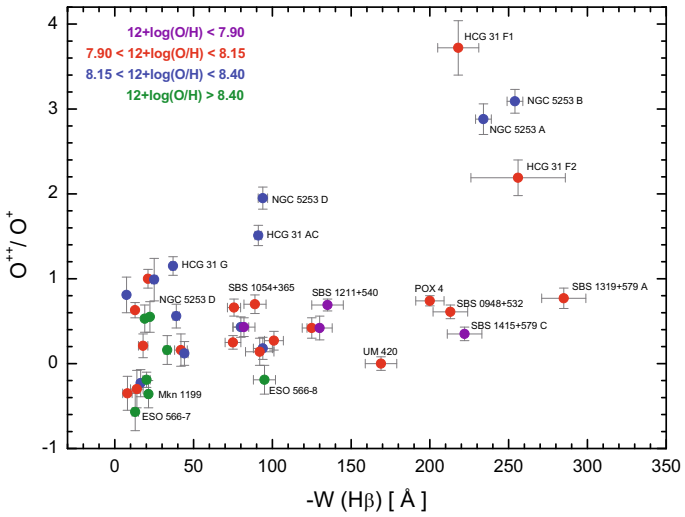

Fig. 6. O^{++}/O^{+} ratio vs. W(Hβ). The colour-dots indicate the oxygen abundance range of each object. Some objects have been labeled.

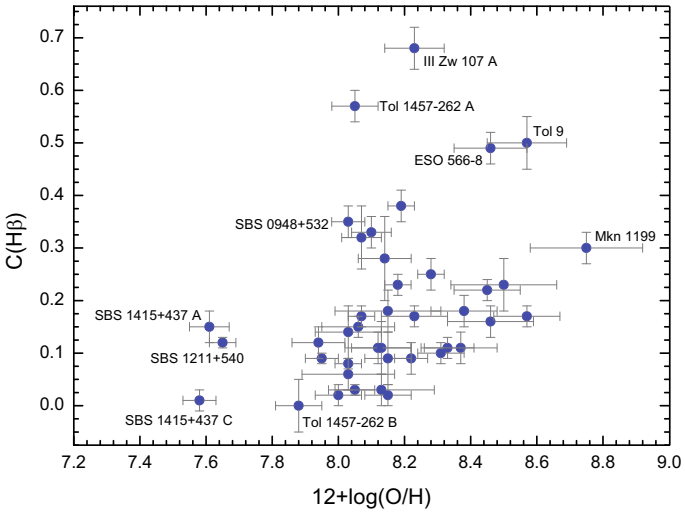

Fig. 7. Reddening coefficient, c(Hβ), vs. the oxygen abundance for the regions analysed in this work. Some objects have been labeled.

This indicates that younger bursts have a larger ionization budgets and are therefore capable to heat the ionized gas to higher electron temperatures. Another effect that we should considered here is that galaxies with higher metallicity (and hence with lower electron temperature) usually have a higher absorption in the Hβ line than low-metallicity objects because of older stellar populations. Indeed, it is interesting to note that objects in the metallicity range $7.90 < 12 + \log(\mathrm{O/H}) < 8.15$ may have any value of W(Hβ). This is very probably because within this metallicity range lie both dwarf objects with no underlying old stellar population (i.e., HCG 31 F, SBS 0948+532) and galaxies which possess a considerable amount of old stars (i.e, HCG 31 B, Mkn 5).

Figure 6 shows that the ionization degree of the ionized gas of the starburts seems to increase with the increasing of $|W(\mathrm{H}\beta)|$. This is a relation similar to that found in Fig. 5 and also indicates that younger bursts harbour a higher proportion of massive stars and therefore their associated H II regions have larger ionization parameters. That is evident in NGC 5253 A, B and HCG 31 F, which show both the highest values of the $|W(\mathrm{H}\beta)|$ and the O^{++}/O^{+} ratio and possess the youngest star-formation bursts (see Table 1). The increasing of the O^{++}/O^{+} ratio as increasing $|W(\mathrm{H}\beta)|$ seems to be independent of the metallicity, although galaxies with higher metallicity tend to show the lowest ionization degrees.

The dependence of the reddening coefficient as a function of other parameters is also interesting. Figure 7 plots c(Hβ) vs. the oxygen abundance. Although the dispersion of the data is rather scattered, we see a clear dependence: the reddening coefficient is higher at higher metallicities. We should expect this result, because galaxies with higher oxygen abundance are chemically more evolved and should contain a larger proportion of dust particles that absorbs the nebular emission.

Another interesting relation is shown in Fig. 8, which plots the equivalent width of the stellar absorption underlying the H I Balmer lines (W_{abs}) as a function of the oxygen abundance. We can see that objects with higher metallicities show larger W_{abs}. More metallic galaxies correspond to more massive and chemically evolved systems, which means that they have consumed

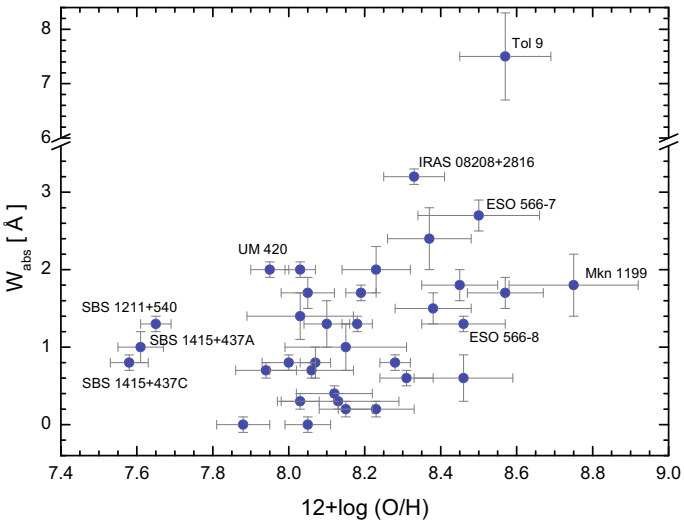

Fig. 8. Equivalent width of the underlying stellar absorption in the Balmer H I lines, W_{abs}, vs. the oxygen abundance for the regions analysed in this work. Notice that the y-axis has been broken for clarity. The value of W_{abs} for UM 420 is very probably overestimated, because this galaxy is observed through the external areas of the spiral disc of the foreground galaxy UCG 01809 (see Fig. 13 in Paper I).

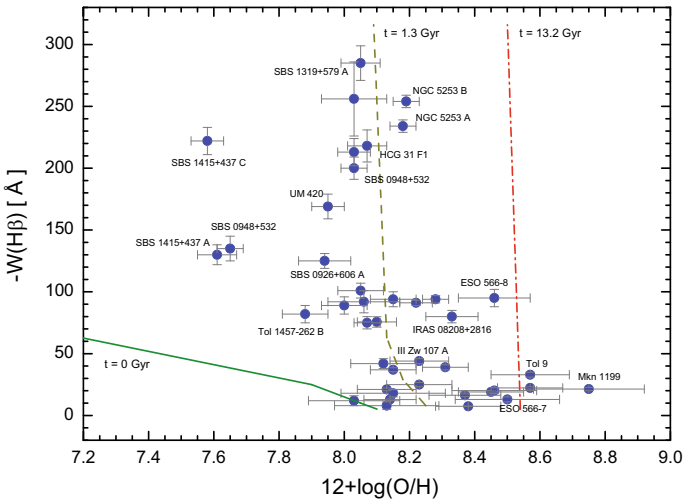

Fig. 9. Hβ equivalent width vs. oxygen abundance. Some objects have been labeled. Some chemical evolution models of H II galaxies provided by Martín-Manjón et al. (2008) are also plotted. See text for details.

a larger fraction of their gas and the stellar component should be comparatively more important. The data corresponding to the lowest metallicity objects analysed in this work (SBS 1415+579 and SBS 1211+540) show a value of W_{abs} relatively high what is to be for them. This suggests a considerable underlying stellar population in these very low-metallicity galaxies, as we already discussed (see Sects. 3.15 and 3.13 of Paper I).

Figure 9 plots W(Hβ) vs. the oxygen abundance. The very large dispersion of W(Hβ) for 12 + log(O/H) of about 8.0 is remarkable, but it also seems clear that galaxies with O/H ratios higher than that value tend to have $|W(H\beta)| \leq 100$ Å and, conversely, galaxies with lower oxygen abundances show $|W(H\beta)| \geq 100$ Å. This behaviour may be be related to the results in Fig. 8, in the sense that more metallic objects tend to have a higher underlying stellar absorption that can lead to an underestimation of $|W(H\beta)|$. Indeed, Fig. 9 also compares our observational data with the predictions given by the chemical evolution models of H II galaxies provided by Martín-Manjón et al. (2008). They assumed the star formation as a set of successive bursts, each galaxy experiencing 11 star-formation bursts along its evolution of 13.2 Gyr. Figure 9 includes the results for the first (t = 0 Gyr), second (t = 1.3 Gyr) and last (t = 13.2 Gyr) bursts for a model that considers an attenuated bursting star-formation mode and that 1/3 of the gas is always used to form stars in each time-step. As we see, all the strong starbursting systems are located between the positions of the first and second burst models, confirming that although the dominant stellar population is certainly very young, previous star-formation events in the last 500–1000 Myr are needed to explain our observational data points. This agrees well with the minimum ages of the underlying stellar component we derived using our photometric data (see Sect. 2 and last column of Table 1). The Martín-Manjón et al. (2008) models also explain the large dispersion of W(Hβ) for 12 + log(O/H) of about 8.0, as well as the trend that more metal rich galaxies have lower values of $|W(H\beta)|$ because of the effects of the underlying stellar populations.

Another indication of the effect of the underlying evolved stellar population is found in Fig. 10, which compares the [O III] λ5007 line flux with the W(Hβ) of the sample galaxies with the model predictions by Schaerer & Leitherer (2001). Although a general good correspondence is found, some of the objects are slightly displaced to the left – lower W(Hβ) – of the models predictions, suggesting that perhaps the measured values of $|W(H\beta)|$ are underestimated for some of them that precisely coincide with those with a larger oxygen abundance, as we also concluded before.

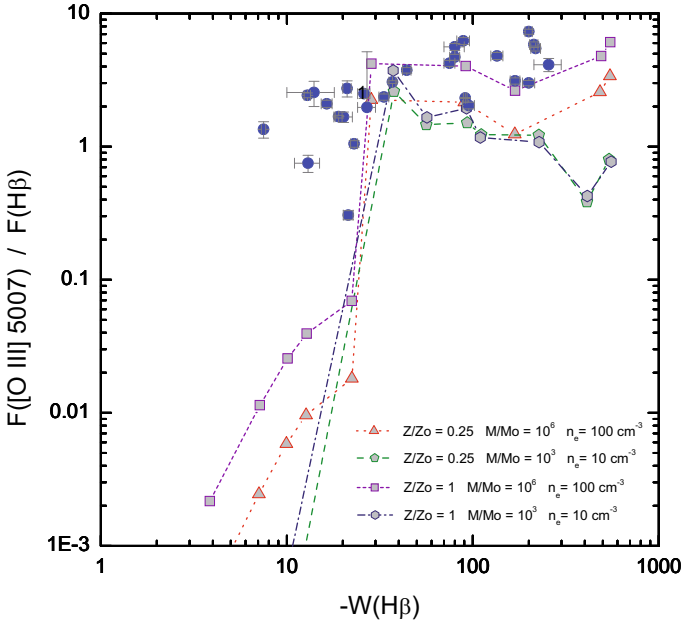

Fig. 10. F([O III] λ5007)/F(Hβ) vs. W(Hβ) and comparison with the predictions given by four different ionization models by Stasińska et al. (2001). See text for details.

4. Chemical abundances of the ionized gas

Table 3 compiles the oxygen abundance, the O^{++}/O^{+} ratio and the N/O, S/O, Ne/O, Ar/O, and Fe/O ratios (all in logarithmic units) for all galaxies analysed in this work. As we already said, 31 up to the 41 independent regions within the WR galaxy

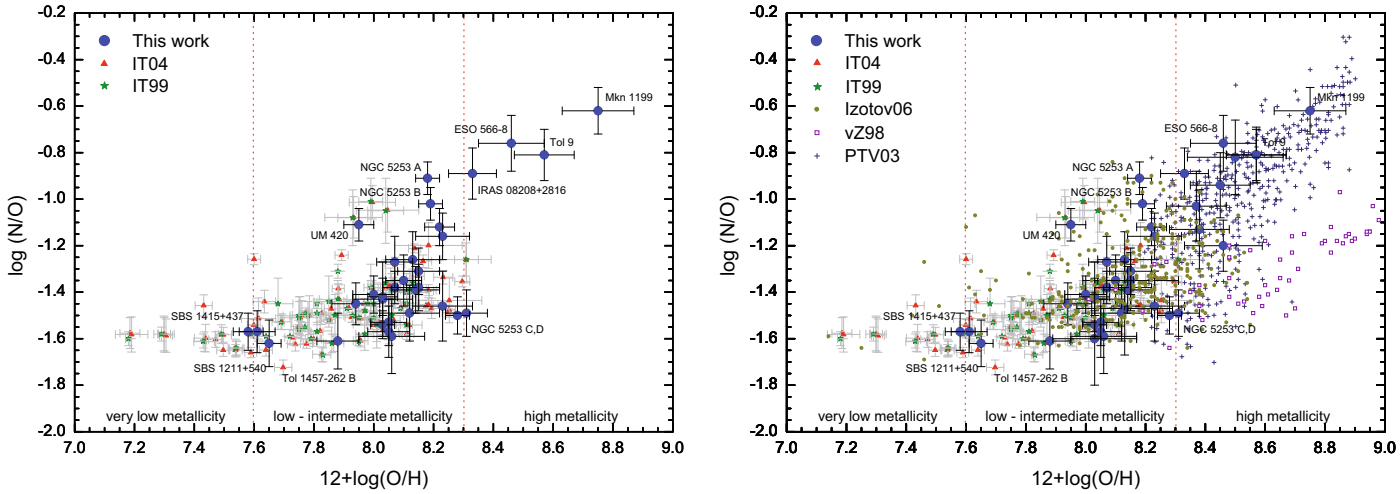

Fig. 11. (*Left*) N/O ratio vs. oxygen abundance for all objects with a direct estimate of T_e. Our data are compared with those compiled by IT99 (Izotov & Thuan 1999) and Izotov et al. (2004). (*Right*) N/O ratio vs. oxygen abundance for all galaxies analysed in this work (also included objects which chemical abundances are derived using empirical calibrations). For comparison, we have included other galaxy samples from the literature whose O/H ratio has been determined using empirical calibrations: Izotov et al. (2004, 2006), van Zee et al. (1998), IT99 (Izotov & Thuan 1999) and PTV03 (Pilyugin et al. 2003).

sample analysed here have a direct estimate of the electron temperature (as indicated in Table 3). Figure 11 (left) plots the N/O ratio vs. the oxygen abundance for all our data with a direct estimate of the electron temperature and its comparison with previous samples involving similar objects and T_e-based (Izotov & Thuan 1999; Izotov et al. 2004). This figure shows that the position of our data agrees with that obtained using other observations. The errors we estimated in our objects are in general higher than those reported by Izotov & Thuan (1999) and Izotov et al. (2004) basically because we used different criteria for estimating observational errors, which are more conservative as well as more realistic in our opinion. We also point out that our data are always of higher spectral and spatial resolution than those obtained by the aforementioned authors, and have a similar or even higher signal-to-noise ratio in many cases. This is an important point to be clarified because non-specialist in the spectra of ionized nebulae may interpret that lower quoted uncertainties are synonymous of better observational data, and this may not always be the case. Although the errors in the electron temperatures derived using the empirical methods are large, relative atomic abundances (such as the N/O ratio) are less sensitive to the choice of T_e. Therefore they are used in many occasions to compare with the results provided by previous observations or with the predictions given by theoretical models.

4.1. The N/O ratio

Figure 11 (right) plots the N/O ratio vs. *abox* for all objects analysed in this work; the chemical abundances were derived either from the direct method or via empirical calibrations. We compare our data with the two galaxy samples previously indicated (Izotov & Thuan 1999; Izotov et al. 2004) and with other galaxy samples whose data have been obtained using empirical calibrations: Izotov et al. Izotov et al. 2006, whose data were extracted from the SDSS, and van Zee et al. (1998), who study data from H II regions within spiral galaxies with chemical abundances computed via the direct method or using the McGaugh 1994 empirical calibration. In some sense, the N/O ratio of a galaxy is an indicator of the time that has elapsed since the bulk of star formation occurred, or of the nominal *age* of the galaxy as suggested by Edmunds & Pagel 1978. Following the position of our data points in Fig. 11 we see that they follow the expected trend:

1. The N/O ratio is rather constant for $12 + \log(O/H) \leq 7.6$. In our case, for the galaxies SBS 1211+540 and SBS 1415+437 we derive $\log N/O \sim -1.6$, similar values as those found by Izotov & Thuan (1999). These authors explained the constant N/O ratio in very low-metallicity objects assuming that the nitrogen is produced only as a primary element in massive, short-life stars. However, other authors have claimed that this may be not completely true (i.e., Henry et al. 2000; Pilyugin et al. 2003; Mollá et al. 2006) because of the lack of a clear mechanism that produces N in massive stars besides the effect or the stellar rotation (Meynet & Maeder 2005). Furthermore, these galaxies already host old stellar populations, and hence low- and intermediate-mass stars should be also releasing N to the ISM. Henry et al. (2000) explained the constancy of the N/O ratio in metal-poor galaxies by a historically low star-formation rate, where almost all the nitrogen is produced by 4–8 $M_\odot$ stars. Additionally, Izotov et al. (2006) suggested that the low dispersion of the data in this part of the diagram is probably explained by the low number of WR stars that are expected at very low-metallicity regimes.
2. However, there is an important dispersion of the data in the interval $7.6 \leq 12 + \log(O/H) \leq 8.3$. This problem has been analysed by several authors in the past (i.e., Kobulnicky & Skillman 1998; Izotov & Thuan 1999; Pilyugin et al. 2003; Mollá et al. 2006). Two main scenarios have been proposed for explaining this dispersion:
   (a) a loss of heavy element via galactic winds. In particular, it should be a loss of α-elements via supernova explosions. α-elements, such as oxygen, are produced in massive short-lived stars (Edmunds & Pagel 1978; Clayton & Pantelaki 1993). Hence, the effect of supernova explosions would produce a underabundance of oxygen (Esteban & Peimbert 1995), increasing the N/O ratio. However, the observational evidence for low-mass galaxies with galactic winds is still unclear (i.e. Marlowe et al. 1995; Bomans et al. 2007; Dubois & Teyssier 2008;

van Eymeren et al. 2008, 2009, 2010) and even the numerical simulations give very discrepant results (i.e., Mac Low & Ferrara 1999; Springel & Hernquist 2003; Tenorio-Tagle et al. 2006; Dubois & Teyssier 2008);

(b) a delayed release of nitrogen and elements produced in low-mass long-lived stars compared to the α-elements. The N/O ratio drops and the O/H ratio increases as supernovae release the α-elements into the ISM. Consequently, the chemical properties of these galaxies would vary very fast (few tens of Myr) during the starburst phase (Kobulnicky & Skillman 1998). The delayed-release hypothesis also predicts that BCDGs with high N/O ratios are experiencing their first burst of massive star formation after a relatively long quiescent interval (oxygen has still not been completely delayed by massive stars and mixed with the surrounding ISM), while those objects with low N/O ratios have had little or no quiescent interval. However, recent chemical evolution models suggest that the releasing and mixing of the oxygen occurs almost instantaneously, and hence the delayed-release scenario cannot explain BCDGs with high N/O ratio. If this is the case, the most plausible explanation of the high N/O ratio observed in these objects is the chemical pollution due to the winds of WR stars, which are indeed ejecting N to the ISM, as we will discuss below.

3. For moderate high-metallicities objects, 12 + log(O/H) $\geq$ 8.3, the N/O ratio clearly increases with increasing oxygen abundance. This trend seems to be a consequence of the metallicity-dependence of nitrogen production in both massive and intermediate-mass stars (e.g., Pilyugin et al. 2003), the N/O ratio increases at higher metallicities. Hence, nitrogen is essentially a secondary element in this metallicity regime (Torres-Peimbert 1989; Vila-Costas & Edmunds 1993; Henry et al. 2000; van Zee & Haynes 2006). Besides the uncertainties (that are higher than those estimated in other objects because the T_e error is higher at higher metallicities) our data agree with the tendency found in other galaxy samples, as that compiled by Pilyugin et al. (2003). However, notice that the galaxy sample compiled by van Zee et al. (1998) does not agree with our data, as her data have a systematically lower N/O ratio. In some cases, differences higher than 0.5 dex in the N/O ratio are found for a particular oxygen abundance. This discrepancy may be partially explained by the fact that empirical calibrations from photoionized models – van Zee et al. (1998) used McGaugh (1991) models – seem to overestimate the actual oxygen abundance by at least 0.2 dex (see below), and hence the derived N/O ratio is lower than the actual value.

In summary, Fig. 11 can be explained assuming the very different star-formation histories that each individual galaxy has experienced (Pilyugin et al. 2003; van Zee & Haynes 2006). A galaxy with a constant SFR will have a lower net N/O yield than a galaxy with declining SFR, because more oxygen has been released into the ISM due to the ongoing star-formation activity. This observational result completely agrees with the predictions given by chemical evolution models that consider the effect of the star-formation history in the N/O–O/H diagram, as those presented by Mollá et al. (2006).

4.2. Nitrogen enrichment in WR galaxies

From Fig. 11, it is evident that there are some objects in the low-intermediate metallicity regime with a higher N/O ratio than expected for their oxygen abundance. An excess of nitrogen abundance has been reported in a few cases (e.g. Kobulnicky et al. 1997; Pustilnik et al. 2004). Remarkably, the common factor observed in all galaxies with a high N/O ratio is the detection of Wolf-Rayet features. Indeed, as we demonstrated in our analysis of NGC 5253 (López-Sánchez et al. 2007), the ejecta of WR stars may be the origin of a localized N (and probably also He) enrichment of the ISM in these galaxies.

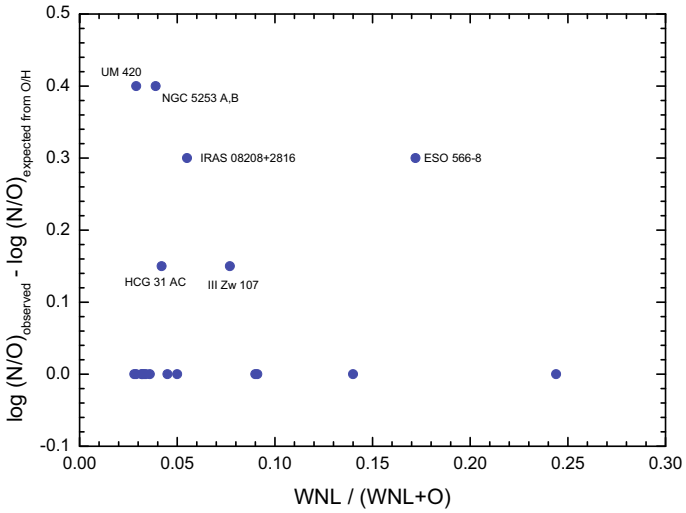

Fig. 12. Observed nitrogen overabundance, $\Delta(N/O) = \log(N/O_{observed}) - \log(N/O_{expected\ from\ O/H})$, vs. the WNL/(WNL+O) ratio for our sample galaxies (derived in Paper III). Some important objects have been labeled.

The analysis of the WR populations within our sample galaxy was performed in Paper III. The numbers of WNL and WCE stars were computed assuming metallicity-dependent WR luminosities (Crowther & Hadfield 2006). We detected the blue WR bump (the broad He II λ4686 emission line) in all objects with high N/O ratio: UM 420, NGC 5253 A,B, HCG 31 AC, IRAS 08208+2816, III Zw 107 and ESO 566-8, indicating that these bursts host an important WNL star population.

Figure 12 plots the observed nitrogen overabundance, $\Delta(N/O) = \log(N/O_{observed}) - \log(N/O_{expected\ from\ O/H})$, as a function of the derived WNL/(WNL+O) ratio. We do not see any clear trend in this diagram, merely that the objects with a high N/O ratio do not show a particularly high WNL/(WNL+O) ratio.

Galaxies HCG 31 AC and III Zw 107 seem to show a slight nitrogen excess [$\Delta(N/O) \sim 0.15$ dex]. Three of the galaxies with high N/O ratio compiled by Pustilnik et al. (2004) are plotted in Fig. 12: NGC 5253 (already discussed), Mkn 1089 (HCG 31 AC) and UM 420. Our data confirm the nitrogen overabundance in UM 420 [$\Delta(N/O) \sim 0.4$ dex], but not a significant N/O ratio in HCG 31 AC [$\Delta(N/O) \sim 0.15$ dex; Pustilnik et al. (2004) quoted ~0.5 dex]. We also find a relatively high N/O ratio in ESO 566-8 [$\Delta(N/O) \sim 0.3$ dex].

The very rare occurrence of objects with a large N overabundance suggests the general idea of the short-time scales for the localized N pollution and its fast dispersal. Brinchmann et al. (2008) used SDSS data to find that for $|W(H\beta)| \geq 100$ Å, WR galaxies show a high N/O compared to non-WR galaxies. Quantitatively these authors found that on average $\Delta \log(N/O)_{[WR-nonWR]} = 0.13 \pm 0.04$. They interpreted this result as a rapid enrichment of the ISM from WR winds. Brinchmann et al. (2008) also found that WR galaxies are in general more metal-rich at a given $|W(H\beta)|$ than similar galaxies without WR

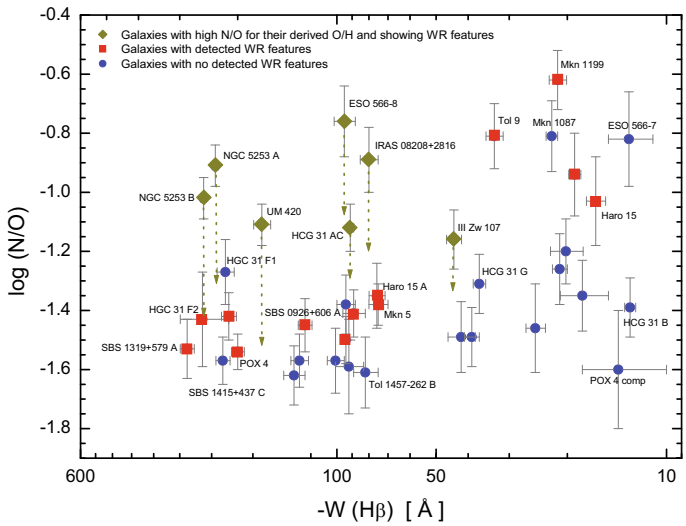

Fig. 13. Hβ equivalent width vs. the N/O ratio. Blue circles indicate regions with no detected WR features. Red squares are galaxies in which WR features are observed. Yellow diamonds correspond to objects with a high N/O ratio for their oxygen abundance, all showing WR features. The Δ(N/O) = log(N/O$_{\rm observed}$) − log(N/O$_{\rm expected\ from\ O/H}$) difference is shown in every galaxy with dotted yellow lines.

features, which likely is a reflection of WR stars being more abundant at higher metallicities (see Fig. 5 of Paper III).

Although we do not dismiss the statistical analysis performed by Brinchmann et al. (2008) comparing WR and non-WR galaxy data, we would like to warn about the use of data with low spectral resolution in order to derive an accurate nitrogen abundance in individual objects. This is commonly done via the analysis of the [N II] λ5683 emission line, very close to Hα. Lack of sufficient spectral resolution will derive a blending of both lines and a probable over-estimation of the [N II] λ5683 flux, that would be even higher if broad low-intensity wings in the Hα profile exist, which are actually rather common in WR galaxies (e.g. Méndez & Esteban 1997). On the other hand, as explained by Izotov et al. (2006), the bright doublet [O II] $\lambda\lambda$3726,3729 is not observed in the SDSS spectra for nearby galaxies, and hence the estimate of the total oxygen abundance has to be done via the [O II] $\lambda\lambda$7319,7330, which is much fainter, very dependent on the electron density and severely affected by sky emission features. Therefore their associated errors are usually larger than for the [O II] $\lambda\lambda$3726,3729 lines. More data and a re-analysis of the chemical abundances in galaxies where WR features are detected, with a similar analysis of a sample of non-WR galaxies, are needed to get any definitive results.

Some authors (i.e. Izotov et al. 2006) suggest that there is a dependence between the N/O ratio and the Hβ equivalent width: the N/O ratio should increase with decreasing $|W(\mathrm{H}\beta)|$. This trend was also observed by Brinchmann et al. (2008), but only for objects with $|W(\mathrm{H}\beta)| \geq 100$ Å. Figure 13 plots the N/O ratio vs. $W(\mathrm{H}\beta)$ for the objects analysed here. In this figure we distinguish between objects with high N/O ratio for their oxygen abundance and WR features (yellow diamonds), and galaxies with a normal N/O ratio with (red squares) or without (blue circles) WR features.

From Fig. 13 it is evident that non-WR galaxies only show high N/O ratios when their $|W(\mathrm{H}\beta)| < 50$ Å. Their N/O ratio becomes low for larger equivalent widths. Brinchmann et al. (2008) suggested that the non-detection of high N/O ratios in objects with small equivalent widths is consistent with very young bursts where the WR stars have not yet had a change to enrich the surrounding ISM to a noticeable degree. However, this is probably a consequence of both the complex star-formation histories and the high relative importance of the old underlying stellar populations in these systems.

On the other hand it is remarkable that the WR galaxies with $|W(\mathrm{H}\beta)| < 50$ Å show systematically high N/O ratios, but a large dispersion when $|W(\mathrm{H}\beta)| > 50$ Å. This dispersion becomes substantially smaller when we consider the N/O ratio expected for their O abundance for those objects with a high Δ(N/O). If the high N/O ratios in these galaxies are produced by the chemical pollution due to winds of WR stars, objects would move to the right in Fig. 13 once the burst is finished because of the decreasing of $|W(\mathrm{H}\beta)|$. If the chemical pollution is very localized, we should also expect that objects with a N excess would move towards lower values of the N/O ratio as the fresh released material is dispersed and mixed with the existing gas of the galaxy. Hence, detailed analyses of galaxies with a localized high N/O ratio, such as we performed in NGC 5253 (López-Sánchez 2007), are fundamental to solve these unsolved questions, which will definitely be key elements to the evolution of the galaxies.

4.3. The α-elements to oxygen ratio

Figure 14 plots the Ne/O, S/O, Ar/O, and Fe/O ratios as a function of 12 + log(O/H) for all objects analysed in this work. We compare our observational results with those found in samples with similar characteristics (Izotov & Thuan 1999; Izotov et al. 2006). We remark again that although the estimates of our errors are higher than those provided by other samples, they are not a consequence of the quality of our data but derive from the different formalism we used to estimate the uncertainties. In any case, our results completely agree with those previously reported in the literature. The relative abundance ratios of the α-elements (neon, sulfur, and argon) to oxygen are approximately constant, as expected because all four elements (O, Ne, S and Ar) are mainly produced by massive stars. For our sample, the mean log(Ne/O), log(S/O), and log(Ar/O) ratios are -0.70 ± 0.13, -1.68 ± 0.10 and -2.37 ± 0.12, respectively. These values are comparable to the values reported for starbursting dwarf galaxies (e.g., Izotov & Thuan 1999; Izotov et al. 2006) and for other dwarf irregular galaxies (e.g., van Zee et al. 1998; van Zee & Haynes 2006). For example, Izotov & Thuan (1999) found mean values of -0.72 ± 0.06, -1.56 ± 0.06, and -2.26 ± 0.09 for the log(Ne/O), log(S/O), and log(Ar/O) ratios, respectively.

Despite their higher uncertainties, we notice that the Ne/O ratio seems to increase slightly with increasing oxygen abundance. This effect was reported by Izotov et al. (2006), who interpreted it as due to a moderate depletion of oxygen onto grains in the most metal-rich galaxies. Verma et al. (2003) observed an underabundance of sulphur in relatively high-metallicity starburst galaxies. These authors interpreted this effect as a consequence of the depletion of sulphur onto dust grains. However, we do not see any underabundance of sulphur; quite the opposite, the sulphur abundance is well correlated with both neon and argon abundances.

On the other hand, it seems that the Fe/O ratio slightly decreases with increasing oxygen abundance. This effect was previously observed by Izotov et al. (2006), who suggested that it may be a consequence of the iron depletion in dust grains, which is more important for galaxies with higher metallicities.

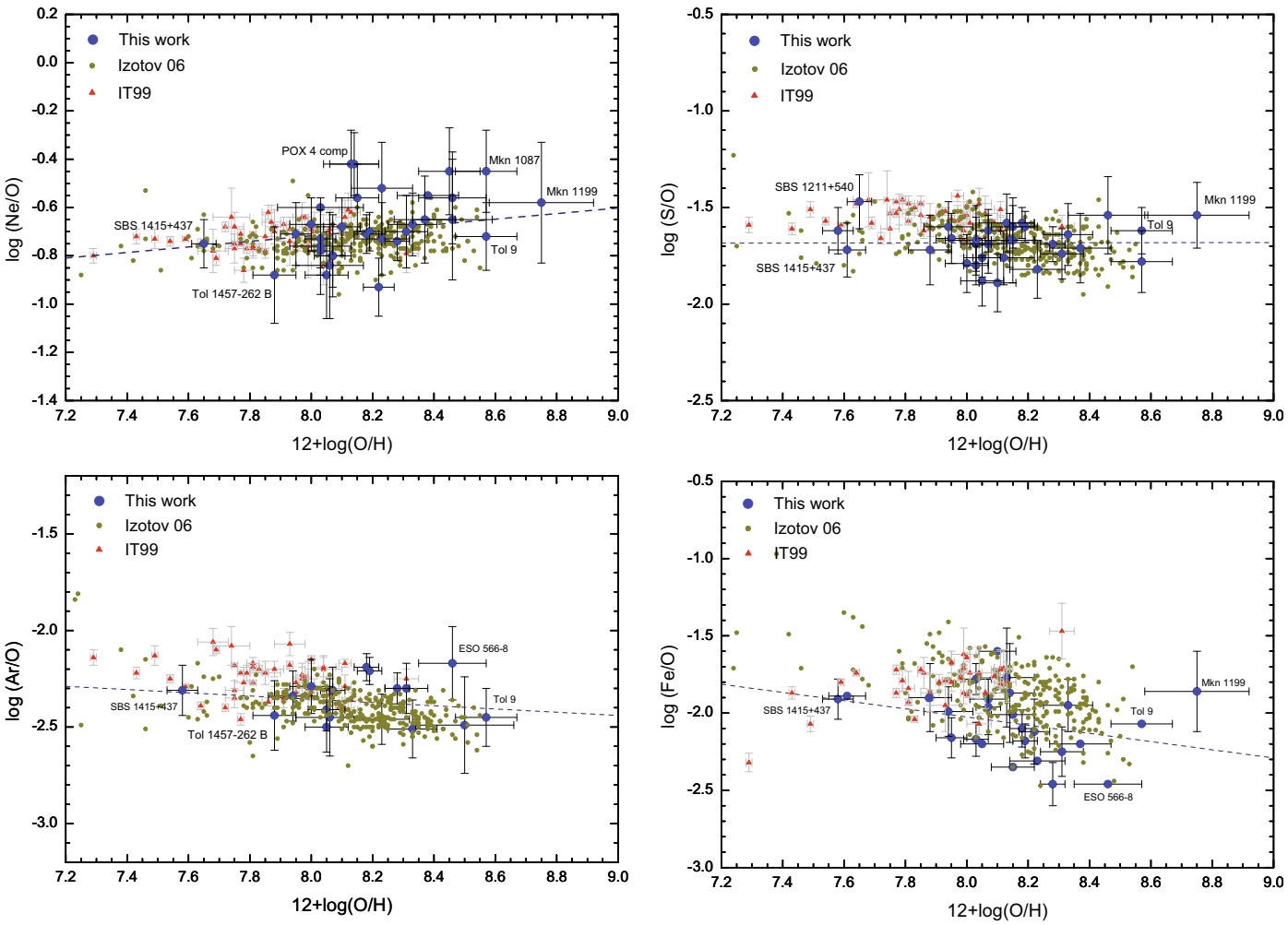

Fig. 14. Ne/O, S/O, Ar/O ang Fe/O ratios vs the oxygen abundance for the galaxies analysed in this work. We compare with the results provided by the galaxy samples considered by Izotov & Thuan (1999) and Izotov et al. (2006). The dashed dark-blue lines indicate a fit to our data.

Finally we remark how important is to use high-quality data and a proper estimate of all the physical parameters (including T_e via the direct method) in an homogeneous sample of objects to get reasonable conclusions about these topics (i.e., this work; Hägele et al. 2008).

4.4. Comparison with empirical calibrations

We used the data of the 31 regions for which we have a direct estimate of T_e and, hence, a direct estimate of the oxygen abundance, to check the reliability of several empirical calibrations. A recent review of 10 metallicity calibrations, including theoretical and empirical methods, was presented by Kewley & Ellison (2008). Appendix A gives an overview of the most common empirical calibrations and defines the typical parameters that are used to estimate the oxygen abundance following these relations. These parameters are ratios between bright emission lines, the most commonly used are R_{23}, P, y, N_2, and O_3N_2 (see definitions in Appendix A). Table A.1 lists the values of all these parameters derived for each region with a direct estimate of the oxygen abundance (see Paper II for details). Table A.1 also includes the value derived for the q parameter (in units of cm s^{-1}) obtained from the optimal calibration provided by Kewley & Dopita (2002). The results for the oxygen abundances derived for each object and empirical calibration are listed in Table A.2. This table also indicates the branch (high or low metallicity) considered in each region when using the R_{23} parameter (see Appendix A), although, as is clearly specified in the table, for some objects with $8.00 \leq 12 + \log(O/H) \leq 8.3$ we assumed the average value found for the lower and upper branches.

Looking at the data compiled in Table A.2 the huge range of oxygen abundance found for the same object using different calibrations is evident. As Kewley & Ellison (2008) concluded, it is critical to use the same metallicity calibration when comparing properties from different data sets or investigate luminosity–metallicity or mass–metallicity relations. Furthermore, abundances derived with such strong-line methods may be significantly biased if the objects under study have different structural properties (hardness of the ionizing radiation field, morphology of the nebulae) than those used to calibrate the methods (Stasińska 2010).

Figures 15 and 16 plots the ten most common calibrations and their comparison with the oxygen abundance obtained using the direct method. We performed a simple statistic analysis of the results to quantify the goodness of these empirical calibrations. Table 4 compiles the average value and the dispersion (in absolute values) of the difference between the abundance given by empirical calibration and that obtained using the direct method. We check that the empirical calibration that provides the best results is that proposed by Pilyugin (2001a,b), which gives oxygen

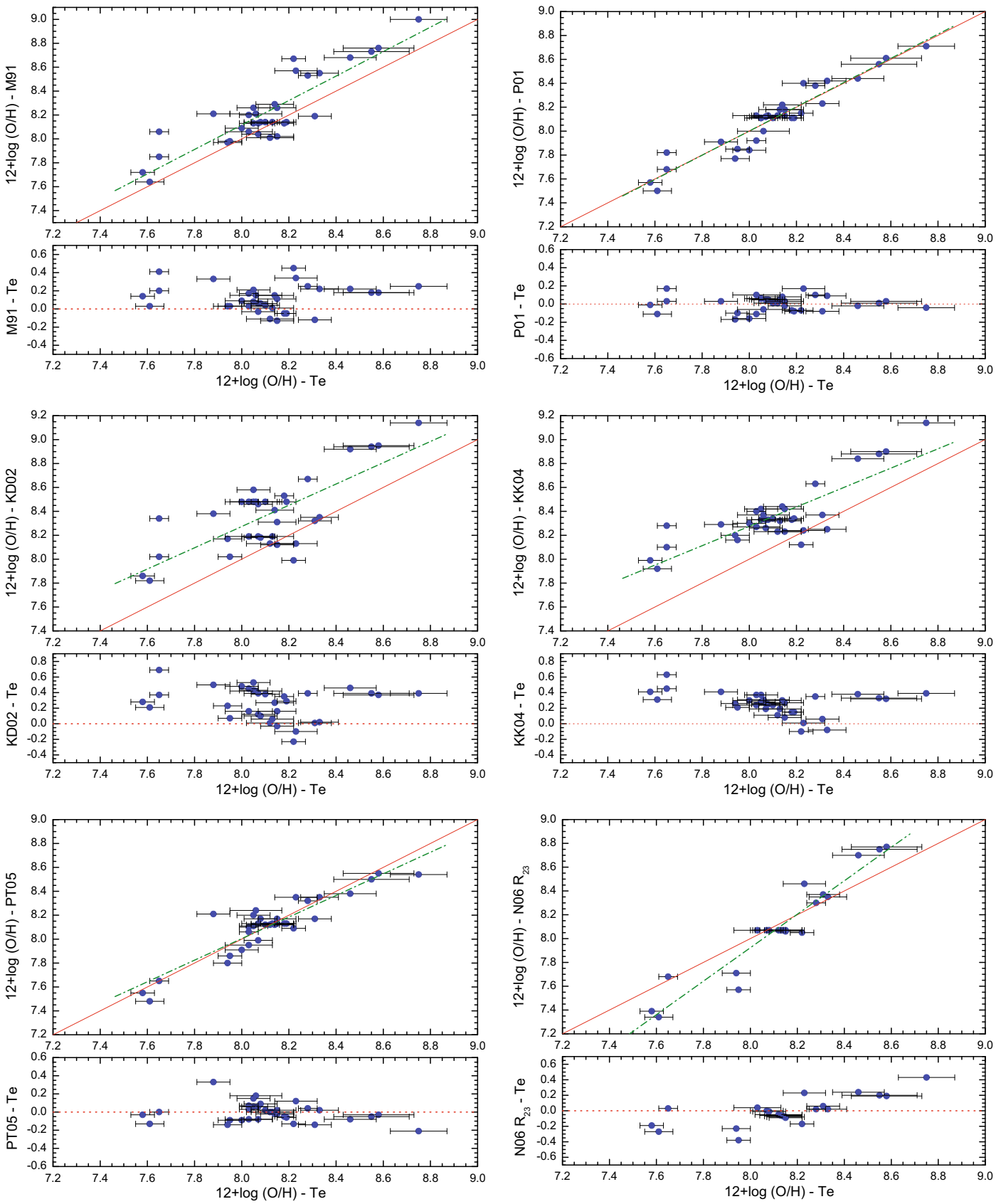

Fig. 15. Comparison between the oxygen abundances derived using the direct method (T_e, always plotted in the x-axis) with those estimated using six different empirical calibrations that consider the R_{23} parameter: M91: McGaugh (1991); P01: Pilyugin (2001a,b); KD02: Kewley & Dopita (2002); KK04: Kobulnicky & Kewley (2004); PT05: Pilyugin & Thuan (2005); N06: Nagao et al. (2006). The *bottom panel* of each diagram indicates the difference between empirical and direct data.

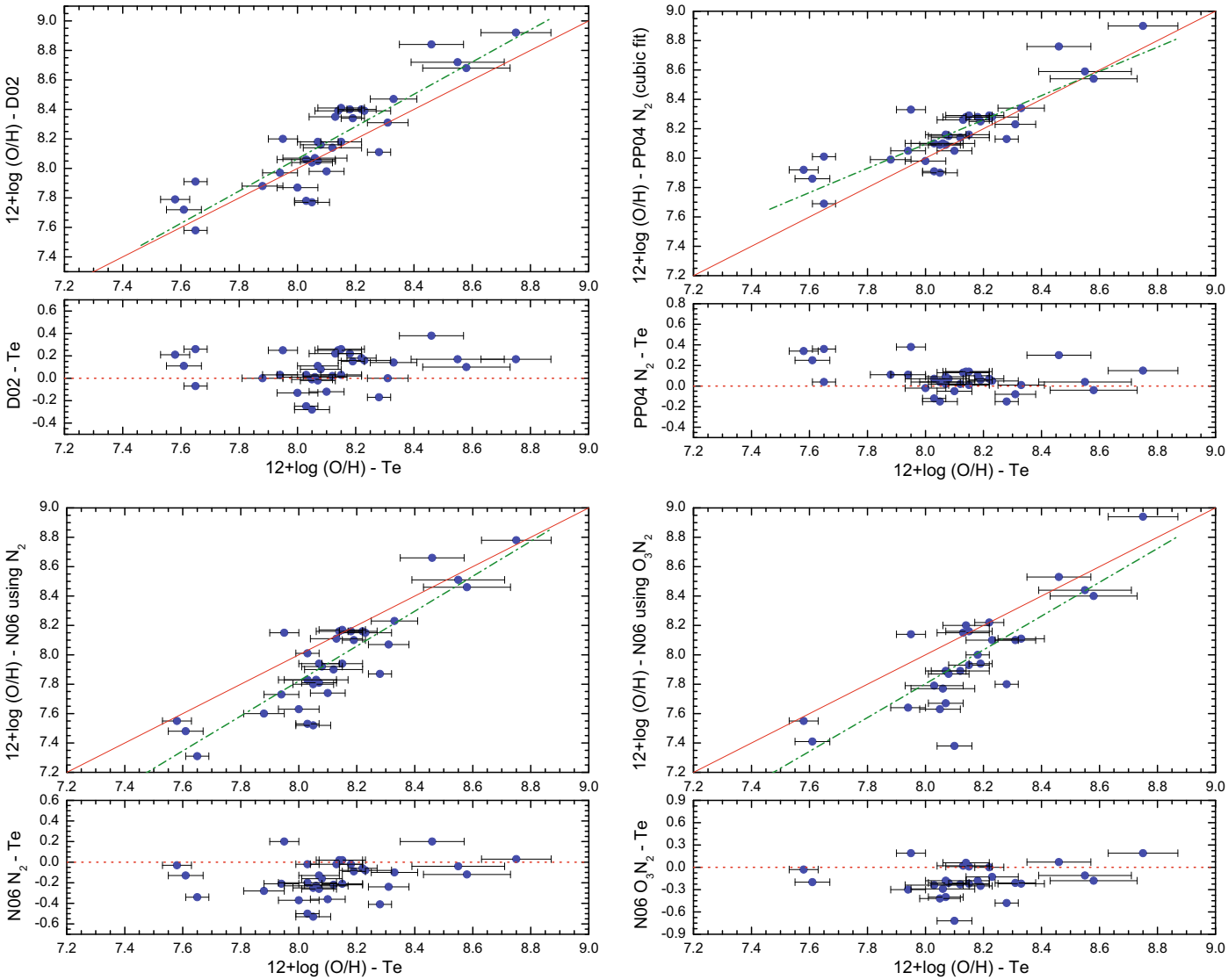

Fig. 16. Comparison between the oxygen abundances derived using the direct method (T_e, in the *x*-axis) with those computed using the calibrations using the N_2 parameter – D02: Denicoló et al. (2002); PP04b: Pettini & Pagel (2004) considering their cubic fit to N_2; N06: Nagao et al. (2006) – and the O_3N_2 parameter following the cubic fit provided by Nagao et al. (2006). The *bottom panel* of each diagram indicates the difference between empirical and direct data.

abundances very close to the direct values (the differences are lower than 0.1 dex in the majority of the objects), and furthermore it possesses a low dispersion. We note however that the largest divergences found using this calibration are in the low-metallicity regime. The update of this calibration presented by Pilyugin & Thuan (2005) seems to partially solve this problem, the abundances provided by this calibration also agree very well with those derived following the direct method. We therefore conclude that the Pilyugin & Thuan (2005) calibration is nowadays the best suitable method to derive the oxygen abundance of star-forming galaxies when auroral lines are not observed.

On the other hand, the results given by the empirical calibrations provided by McGaugh (1991), Kewley & Dopita (2002) and Kobulnicky & Kewley (2004), that are based on photoionization models, are systematically higher than the values derived from the direct method. This effect is even more marked in the last two calibrations, which usually are between 0.2 and 0.3 dex higher than the expected values. These empirical calibrations also have a higher dispersion than that estimated for Pilyugin (2001a,b) or Pilyugin & Thuan (2005) calibrations. Yin et al. (2007) also found high discrepancies when comparing the theoretical metallicities using the theoretical models of Tremonti et al. (2004) with the T_e-based metallicites obtained from Pilyugin (2001a,b) and Pilyugin & Thuan (2005).

One of the possible explanations for the different metallicities obtained between the direct method and those derived from the empirical calibrations based on photoionization models are temperature fluctuations in the ionized gas. Temperature gradients or fluctuations indeed cause the true metallicities based on the T_e-method to be underestimated (i.e. Peimbert 1967; Stasinska 2002, 2005; Peimbert et al. 2007). Temperature fluctuations can also explain our results for NGC 5253 (López-Sánchez et al. 2007): the ionic abundances of O^{++}/H^+ and C^{++}/H^+ derived from recombination lines are systematically 0.2–0.3 dex higher than those determined from the direct method –based on the intensity ratios of collisionally excited lines. This abundance discrepancy has been also found in Galactic (García-Rojas & Esteban 2007) and other extragalactic (Esteban et al. 2009) H II regions and interestingly this discrepancy is in all cases of the same order as the differences between abundances

Table 4. Results of the comparison between the oxygen abundance given by several empirical calibrations and the oxygen abundance derived here following the direct (T_e) method.

Parameter	R_{23}						N_2			O_3N_2	
calibration[a]	P01	PT05	N06	M91	KD02	KK04	D02	PP04	N06	PP04	N06
Average[b]	0.07	0.08	0.14	0.15	0.28	0.27	0.14	0.12	0.18	0.12	0.21
σ[c]	0.05	0.07	0.12	0.11	0.18	0.13	0.10	0.10	0.14	0.10	0.16
Notes[d]	B/A (1)	B/A	(2)	S.H.	S.H.	S.H.	S.H. (3)	B/A (4)	S.L.(5)	B/A (6)	S.L.

Notes. [(a)] The names of the calibrations are the same as in Table A.2. [(b)] Average value (in absolute values) of the difference between the abundance given by empirical calibrations and that obtained using the direct method. The names of the calibrations are the same as in Table A.2. [(c)] Dispersion (in absolute values) of the difference between the abundance given by empirical calibrations and that obtained using the direct method. [(d)] We indicate if the empirical calibration gives results both below and above the direct value (B/A), if they are systematically higher than the direct value (S.H.) or if they are systematically lower than the direct value (S.L.). Some additional notes are: (1) Higher deviation in the low branch. (2) This calibration provides lower oxygen abundances in low-metallicity regions and higher oxygen abundances in high-metallicity regions. (3) Systematically higher only for 12 + log(O/H) > 8.2. (4) Higher deviation for 12 + log(O/H) < 8.0. Considering 12 + log(O/H) > 8.0, we get average = 0.08 and σ = 0.06. (5) Higher deviation at lower oxygen abundances. (6) Higher deviation for 12 + log(O/H) < 8.0. Assuming 12 + log(O/H) > 8.0, average = 0.09 and σ = 0.06.

derived from the direct methods and empirical calibrations based on photoionization models.

The conclusion that temperature fluctuations do exist in the ionized gas of starburst galaxies is very important for the analysis of the chemical evolution of galaxies and the Universe. Indeed, if that is correct, the majority of the abundance determinations in extragalactic objects following the direct method, including those provided in this work, have been underestimated by at least 0.2 to 0.3 dex. Deeper observations of a large sample of star-forming galaxies – that allow us to detect the faint recombination lines, such as those provided by Esteban et al. (2009) – and more theoretical work – including a better understanding of the photoionization models, such as the analysis provided by Kewley & Ellison (2008) – are needed to confirm this puzzling result.

On the other hand, we have checked the validity of the recent relation provided by Nagao et al. (2006), which merely considers a cubic fit between the R_{23} parameter and the oxygen abundance. This calibration was obtained combining data from several large galaxy samples, the majority from the SDSS, which includes all kinds of star-forming objects. As it is clearly seen in Table A.2 and in Fig. 16, the Nagao et al. (2006) relation is not suitable to derive a proper estimate of the oxygen abundance for the majority of the objects in our galaxy sample. In general, this calibration provides lower oxygen abundances in low-metallicity regions and higher oxygen abundances in high-metallicity regions. Objects located in the metallicity range 8.00 ≤ 12 + log(O/H) ≤ 8.15 have systematically 12 + $\log(O/H)_{N06}$ ∼ 8.07 because we have to use an average value between the low and the high branches. Furthermore, many of the regions do not have a formal solution to the Nagao et al. (2006) equation, such as the maximum value for R_{23} is 8.39 at 12 + log(O/H) = 8.07. We consider that the use of an ionization parameter – P as introduced by Pilyugin (2001a,b) or q as followed by Kewley & Dopita (2002) – is fundamental to obtain a real estimate of the oxygen abundance in star-forming galaxies, especially in objects showing strong starbursts. In the same sense, the direct method and not the formulae provided by Izotov et al. (2006) (which assumes a low-density approximation in order not to have to solve the statistical equilibrium equations of the O^{+2} ion) provides a good approximation to the actual oxygen abundance when the auroral line [O III] λ4653 is observed.

Empirical calibrations considering a linear fit to the N_2 ratio (Denicoló et al. 2002; Pettini & Pagel 2004) give results that are systematically ∼0.15 dex higher that the oxygen abundances derived from the direct method. The difference is higher at higher metallicities. We do not consider that this trend is a consequence of comparing different objects: both Denicoló et al. (2002) and Pettini & Pagel (2004) calibrations are obtained using a sample of star-forming galaxies similar to those analysed in this work, many of which are WR galaxies. Denicoló et al. (2002) compared the N_2 ratio with the ionization parameter together with the results of photoionization models and concluded that most of the observed trend of N_2 with the oxygen abundance is caused by metallicity changes. The cubic fit to N_2 performed by Pettini & Pagel (2004) better reproduces the oxygen abundance, especially in the intermediate- and high-metallicity regime (12 + log(O/H) > 8.0), where it has an average error of ∼0.08 dex. However, the cubic fit to N_2 provided by Nagao et al. (2006) gives systematically lower values for the oxygen abundance than those derived using the direct method, having an average error of ∼0.18 dex.

The empirical calibration between the oxygen abundance and the O_3N_2 parameter proposed by Pettini & Pagel (2004) gives acceptable results for objects with 12 + log(O/H) > 8.0, with the average error ∼0.1 dex. However, the new relation provided by Nagao et al. (2006) involving the O_3N_2 parameter gives systematically lower values for the oxygen abundance. As we commented before, we consider that the Nagao et al. (2006) calibrations are not suitable for studying galaxies with strong star-formation bursts. Their procedures must be taken with caution, galaxies with different ionization parameters, different chemical evolution histories, and different star formation histories should have different relations between the bright emission lines and the oxygen abundance. This issue is even more important when estimating the metallicities of intermediate- and high-redshift galaxies, because the majority of their properties are highly unknown.

5. Metallicity–luminosity relations

The metallicity of normal disc galaxies is strongly correlated with the galaxy mass. The first mass–metallicity relation was found for irregular and blue compact galaxies (Lequeux et al. 1979; Kinman & Davidson 1981). However, luminosity is often used instead of mass because obtaining reliable mass estimates is difficult. Rubin et al. (1984) provided the first evidence that metallicity is correlated with luminosity in disk galaxies. Further work using larger samples of nearby disk galaxies confirmed

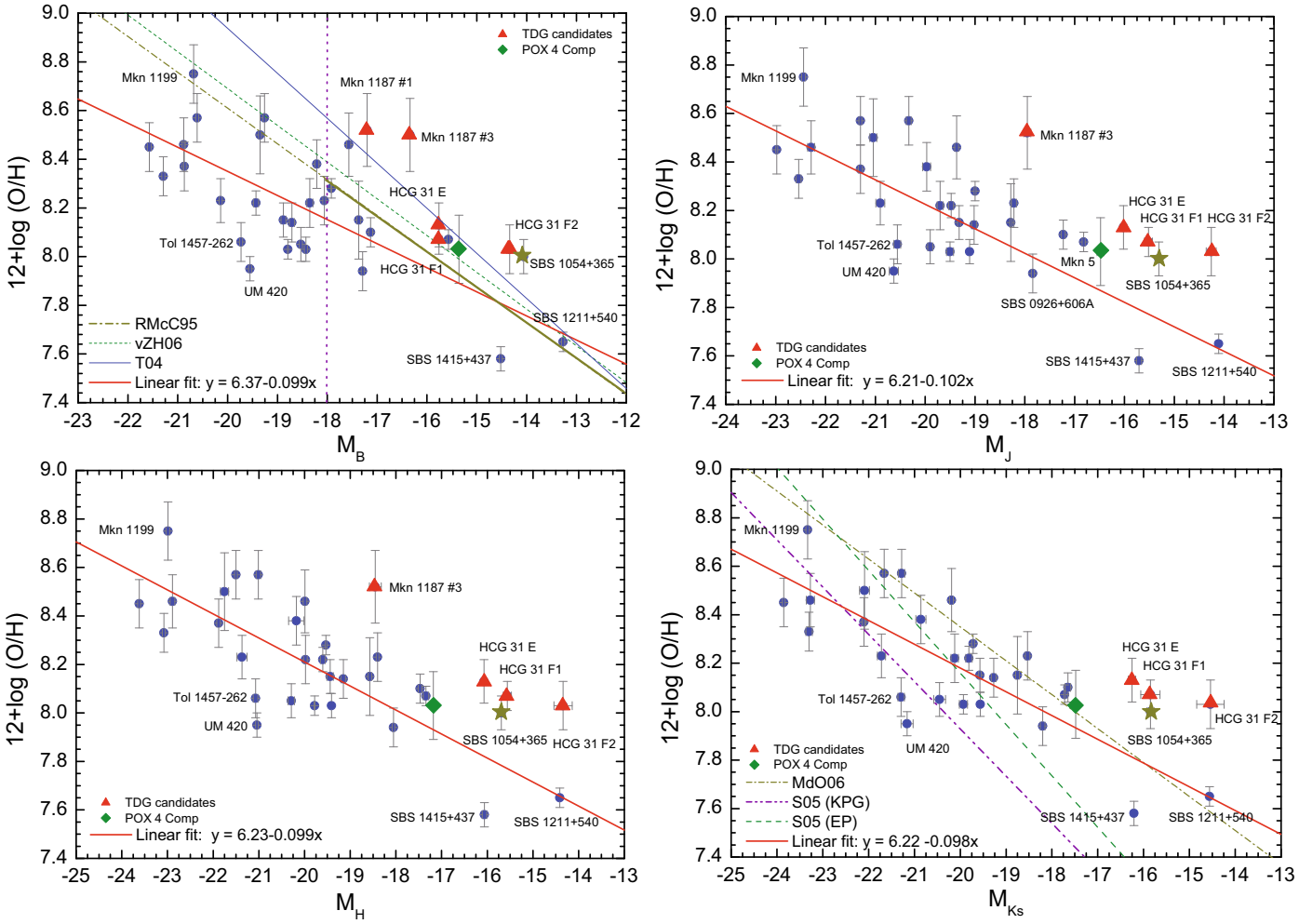

Fig. 17. Metallicity–luminosity diagrams for the objects analysed in this work. The oxygen abundance is expressed in units of 12 + log(O/H); the luminosity is expressed as the absolute magnitude in B, J, H and K_S filters. Red triangles represent the TDG candidates found in HCG 31 (López-Sánchez et al. 2004a) and Mkn 1087 (López-Sánchez et al. 2004b). A green diamond corresponds to the dwarf object surrounding POX 4, while a yellow star indicates the galaxy SBS 1054+365. Linear fits to our data are shown with a continuous red line in the four panels. The M_B–O/H diagram includes the relation derived by Richer & McCall (1995) (continuous dark yellow line) extrapolated to high luminosities (dashed-dotted dark yellow line), the relation provided by van Zee & Haynes (2006) (dashed green line), and the relation derived by Tremonti et al. (2004) using SDSS data (dotted blue line). The M_{K_S}–O/H diagram includes the two relations found by Salzer et al. (2005), one considering the Edmunds & Pagel (1984) calibration (EP, dashed green line) and another assuming the relationships provided by Kennicutt et al. (2003) (KPG, dashed-dotted purple line), and the relation found by Mendes de Oliveira et al. (2006) (dashed-dotted yellow line).

this result (Bothum et al. 1984; Wyse & Silk 1985; Skillman et al. 1989; Vila-Costas & Edmunds 1992; Zaritsky et al. 1994; Garnett 2002). Despite the huge observational effort, the origin of the luminosity–metallicity is still not well understood. The two basic ideas are (i) it represents an evolutionary sequence – more luminous galaxies have processed a larger fraction of their raw materials (McGaugh & deBlok 1997; Bell & deJong 2000; Boselli et al. 2001) – or (ii) it is related to a mass-retention sequence – more massive galaxies retain a larger fraction of their processed material (Garnett 2002; Tremonti et al. 2004; Salzer et al. 2005). Furthermore, other factors may play a key role in the variation of the metal content of a galaxy, remarking the quick metal enrichment that strong star-formation events in dwarf galaxies, such as BCDGs, may experience. In these objects, the freshly processed material may be expelled into the intergalactic medium via galactic winds or be mixed with the reservoirs of non-synthesized gas, in both cases decreasing the global metallicity of the galaxy.

In addition, luminosity–metallicity relations are very useful to discern between pre-existing dwarf galaxies and tidal dwarf galaxy (TDG) candidates (Duc & Mirabel 1998; Duc et al. 2000) because these objects should have a metallicity similar to that observed in their parent spiral galaxies (Weilbacher et al. 2003) and not a low-metallicity as it is found in dwarf objects.

We studied the metallicity–luminosity relation using the data provided by our analysis. Figure 17 plots the oxygen abundance vs absolute magnitude in B and NIR filters and including some relationships found by previous studies. In this figure we distinguish between galaxies (blue points) and TDGs candidates (red triangles) found in HCG 31 and Mkn 1087 groups. We also distinguish the dwarf object surrounding POX 4 (labeled POX 4 comp in figures and tables) because it may be another TDG, and the galaxy SBS 1054+365 because, as we will see later, its position in the metallicity–luminosity diagrams is quite unusual. We estimated the NIR absolute magnitudes for SBS 0948+532 and SBS 1211+540 assuming $V - J \sim 0.8$,

$J - H \sim 0.3$ and $H - K_s \sim 0.15$, that are the average values found in objects with properties similar to these two galaxies (see Paper I).

The M_B–O/H diagram includes the relation given by Richer & McCall (1995) for dwarf and irregular galaxies ($M_B \geq -18$) extrapolated to high luminosities and the van Zee & Haynes (2006) relation found for isolated dwarf irregular galaxies. Both relations have a similar slope (−0.147 and −0.149, respectively) and intercept (5.67 and 5.65, respectively). Our observational data have a rather high dispersion, but the tendency of increasing oxygen abundance with increasing absolute B-magnitude is clear. Most of the objects fainter than $M_B = -18$ are located above those relations, but many of them are TDG candidates. On the other hand, a substantial fraction of the brighter objects tend to be clearly below the metallicity–luminosity relations obtained by previous authors. The best linear fit to our data excluding the TDG candidates – it is well-known that they should not follow the metallicity–luminosity relation (Duc & Mirabel 1998) – provides a slope of -0.099 ± 0.019 and an intercept of 6.37 ± 0.37. The slope we derive for our galaxy sample is shallower than those provided by the Richer & McCall (1995) and van Zee & Haynes (2006) relations. However, the Tremonti et al. (2004) M_B–O/H relation for all kinds of galaxies using SDSS data (plotted with a blue dotted line in Fig. 17) show the steepest slope of all relations, which has a value of −0.185. That disagree with the conclusions reached by Tremonti et al. (2004), who explained the flattening of the $M - Z$ relation at higher masses because efficient galactic winds are able to remove metals from low-mass galaxies.

Some authors (Campos-Aguilar et al. 1993; Peña & Ayala 1993; McGaugh 1994) have already questioned the validity of the luminosity–metallicity relation in starbursting galaxies. As we explained in previous papers (López-Sánchez et al. 2004a,b), we consider that the emission of the dominant young stellar population in these galaxies is increasing their B-luminosity, and hence the use of the standard metallicity–luminosity relation is not appropriate for starburst-dominated galaxies. Indeed, the increment of the B-luminosity is moving all star-forming objects away – towards more negative magnitudes – from the usual relations valid for non-starbursting galaxies, and even producing – incidentally – the TDG candidates to agree with the relations.

As proposed by Hidalgo-Gámez & Olofsson (1998) and reviewed by Salzer et al. (2005), perhaps *NIR* magnitudes are more suitable than the optical B-magnitude to built metallicity–luminosity diagrams. Indeed, *NIR* magnitudes are less affected by extinction and more directly related to the stellar mass of the galaxy than the optical luminosities. Furthermore, the effect of variations in star-formation histories and stellar populations is less pronounced in the *NIR* than in the optical. We analysed the behaviour of the oxygen abundance with the J, H and K_S absolute magnitudes (see Fig. 17). As we expected, the oxygen abundance increases with the luminosity. The slopes, -0.102 ± 0.017, -0.099 ± 0.016, and -0.098 ± 0.015 for M_J, M_H, and M_{K_S}, respectively, and intercepts, 6.21 ± 0.34, 6.23 ± 0.33, and 6.22 ± 0.31, of the lineal fits are remarkably similar to the fit parameters of our M_B–O/H relation. However, these fits have a better correlation coefficient (0.773, 0.779 and 0.790) and dispersion (0.18, 0.17 and 0.17) than those derived for the M_B–O/H relation ($r = 0.719$ and $\sigma = 0.20$). Salzer et al. (2005) found a notable decreasing of the rms scatter of the metallicity–luminosity relation between the blue and the *NIR*.

The M_{K_S}–O/H diagram shown in Fig. 17 includes the relations obtained by Salzer et al. (2005) –which consider two different empirical calibrations of their oxygen abundance, one following the Edmunds & Pagel (1984) method and another considering the Kennicutt et al. (2003) relationships – and Mendes de Oliveira (2006). These relationships have a very different slope (−0.212, −0.195, and −0.14, respectively) and intercept (3.919, 4.029, and 5.55, respectively) than that derived in our analysis of the M_{K_S}–O/H relation. However, for objects with $M_{K_S} < -19$, the relations provided by Salzer et al. (2005) agree fairly well with the position of our data points. These authors found that the slopes of the metallicity–luminosity relations change systematically from the shortest to the longest wavelengths, in that the relation is steepest in the blue and more shallow in the *NIR*. In fact, Salzer et al. (2005) also noted that their derived M_B–O/H relation has a much steeper slope than those found by previously relations (i.e., Skillman et al. 1989, Richer & McCall 1995).

The disagreement between our data and previous metallicity–luminosity relations may arise because our sample was chosen considering WR galaxies, which host strong starbursts, while other samples consider any star-forming galaxies. It may also occur because dwarf galaxies and *normal* galaxies have different relations (i.e. Tremonti et al. 2004). Another fact that can contribute to the aforementioned disagreement is that the oxygen abundances derived in previous analyses have been usually computed via photoionization-based empirical calibrations. As we discussed before, they seem to overestimate the actual O/H ratio by about 0.2 dex.

In Fig. 17 we can see that the separation between the positions of TDG candidates and dwarf galaxies is somewhat more evident in the metallicity–luminosity diagrams involving *NIR* magnitudes. POX 4 comp agrees with the relations, and hence further analysis of this object is needed to understand its real nature. On the other hand, SBS 1054+365 has a higher oxygen abundance for its optical and *NIR* absolute luminosities. We do not consider the O/H to be overestimated because of the high quality of our spectra (Paper II) and because previous studies derived the same metallicity (i.e., Izotov & Thuan 1998). We are also quite confident of the correct determination of its optical and *NIR* magnitudes because of the detailed analysis we already presented in Paper I. Hence we consider that this nearby (8 Mpc) BCDG may have experienced a recent a strong pollution of heavy elements which probably has not had enough time to disperse and mix with the surrounding ISM. In Paper V we will see that this galaxy also possesses a very high $M_{\rm dyn}/L_B$ ratio, suggesting that the neutral gas is quite disturbed. Further analysis of this intriguing object, including H I radio data and optical spectroscopy, would be necessary to ascertain its true nature.

Finally, another aspect that should also be addressed is the possibility that some of the sample objects may be a recent merger of two galaxies. In this case, the integrated luminosity would be higher than that expected for a single galaxy, and hence its position would be also far from the metallicity–luminosity relations. That may be happening in UM 420 – see Sect. 3.9 in Paper I, Sect. 3.9.3 in Paper II and James et al. (2009) – and Tol 1457-262 (see Sect. 3.18.3 in Paper II), which show a considerable high luminosity given their low oxygen abundances. Hence it is more appropriate to compare the stellar mass (and not the B or the *NIR* luminosities) with the metallicity to reach any conclusions about this topic, as we will explain in Paper V.

The nitrogen abundance also has a strong correlation with the luminosity. Figure 18 plots the nitrogen abundance, expressed in units of 12+log(N/H), as a function of the absolute B and K_S magnitudes. As in Fig. 17, we distinguish the TDG candidates and the intriguing objects POX 4 comp and SBS 1054+365. From Fig. 18 it is also evident that the

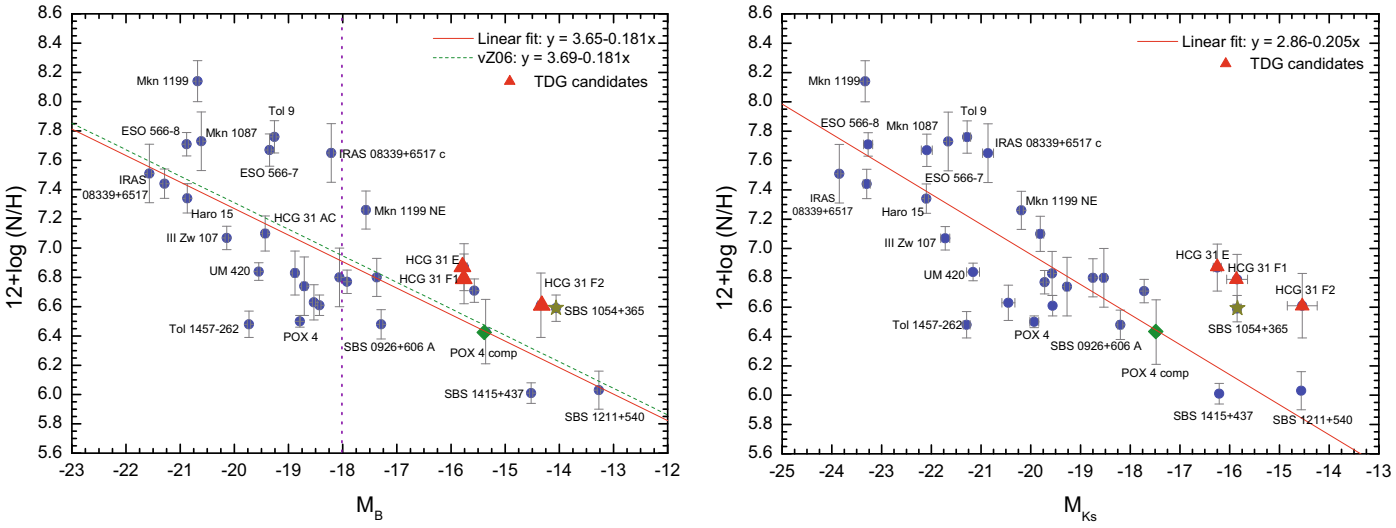

Fig. 18. Nitrogen abundance vs. luminosity for the galaxies analysed in this work. The nitrogen abundance is expressed in units of 12+log(N/H); the luminosity is expressed as the absolute magnitude in B (*left*) and K_S (*right*) filters. Red triangles represent the TDG candidates found in HCG 31 (López-Sánchez et al. 2004a) and Mkn 1087 (López-Sánchez et al. 2004b). A green diamond corresponds to the dwarf object surrounding POX 4, while a yellow star indicates the galaxy SBS 1054+365. The relation derived van Zee & Haynes (2006) is plotted in the M_B-N/H relation with a green dashed line. The fits to our data are shown with a continuous red line.

nitrogen abundance increases with increasing luminosity. We performed a linear fit to our data (without considering the problematic objects already discussed), which is plotted with a continuous red line. In the M_B–N/H diagram this fit yields a slope of -0.181 ± 0.036 and an intercept of 3.65 ± 0.68. This result is virtually identical to that found by van Zee & Haynes (2006), their relation is shown with a green dashed line in the left diagram of Fig. 18. The scatter of the M_B–N/H relation is higher than that found in the M_B–O/H relation, actually, we may distinguish between two kinds of objects in this figure, because the more evolved galaxies (such as Mkn 1199, Mkn 1087, Tol 9, ESO 566-8) and the non-starbursting systems (Mkn 1199 NE, IRAS 08339+6517 c, ESO 566-7) have a higher N/H value at a given absolute B-luminosity than the very starbursting (i.e. IRAS 08339+6517, HCG 31 AC) and blue compact dwarf (i.e. UM 420, POX 4, SBS 0926+606 A) galaxies. TDG candidates do not lie far from this relation. These differences are probably a consequence of the different star-formation histories of the galaxies, as we also explained the scatter in the observed N/O ratio at $12 + \log(\mathrm{O/H}) > 7.9$ (see Fig. 11).

As it happened in the previous diagrams involving the oxygen abundance, the luminosity–metallicity diagram using *NIR* data has a smaller scatter (Fig. 18, right). The fit to our data in the M_{K_S}–N/H diagram, neglecting TDG candidates and problematic objects, gives a slope of -0.205 ± 0.030 and an intercept of 2.86 ± 0.61. The correlation coefficient is $r = 0.813$ and the dispersion is $\sigma = 0.33$. In comparison, the M_B–N/H diagram has $r = 0.707$ and $\sigma = 0.40$. We note that again TDG candidates and the galaxy SBS 1054+365 lie far from this fit, which is plotted in Fig. 18 (right) with a continuous red line. POX 4 comp agrees quite nicely with the relation. In both diagrams, the position of Tol 1457-262 is far from the relation, having a considerable high luminosity for its N/H ratio. As we already discussed, we consider that this object may correspond to a recent merger of two independent galaxies. Hence we conclude that luminosity–metallicity relations using *NIR* band magnitudes are very suitable to understand galaxy properties and evolution, providing tighter correlations than those relations involving optical magnitudes.

6. Metallicity–colour relations

We analysed the relationship between the optical and *NIR* colours observed in each galaxy and its metallicity. Figure 19 plots the results for all colours (from Table 1) vs. the oxygen abundance and a fit to the data. Although the dispersion is large, the general trend is that galaxies with redder colours have a higher oxygen abundance in their ionized gas. This suggests again the relative importance of the evolved stellar populations existing in the galaxies, and agrees both with models of galaxy evolution (i.e., Leitherer et al. 1999; Bruzual & Charlotte 2003) and previous observational analysis (i.e. Jansen et al. 2000; Lilly et al. 2003). Neglecting other effects (such as extinction), the birth of new generations of stars within a galaxy will continuously increase the number of intermediate and low-mass stars, which are the typical stellar population that constitutes the low-luminosity component in starburst galaxies. Hence it should be expected that as the system evolves – increasing its metallicity – its optical and *NIR* colours are more dominated by the evolved population, and therefore they are redder. Another interesting comment regarding these correlations is to remark how important it is to have an estimate of the metallicity of the galaxies when comparing the optical/*NIR* colours with the predictions of theoretical evolutionary models (see Paper I).

Besides the N/O ratio has a large dispersion in our sample objects, we checked whether a correlation exists between this ratio and the $B - V$ colour. Figure 20 plots both quantities considering the $B - V$ colour of the complete galaxy (left panel) and that derived for the old underlying population (right panel). Both diagrams include a fit to our data (continuous red line). Figure 20 shows the large dispersion of the data points, but there seems to be a suggestion of a tendency of increasing N/O with increasing $B - V$ colour. This tendency does not become clearer when considering the data of the underlying stellar component. However, the relation found using our data disagrees with that obtained by van Zee & Haynes (2006) analysing a sample of dwarf irregular galaxies. We note that they referred to the $B-V$ *colour of the underlying population*, but actually it is just the integrated colour of the galaxy. The significant difference found between both

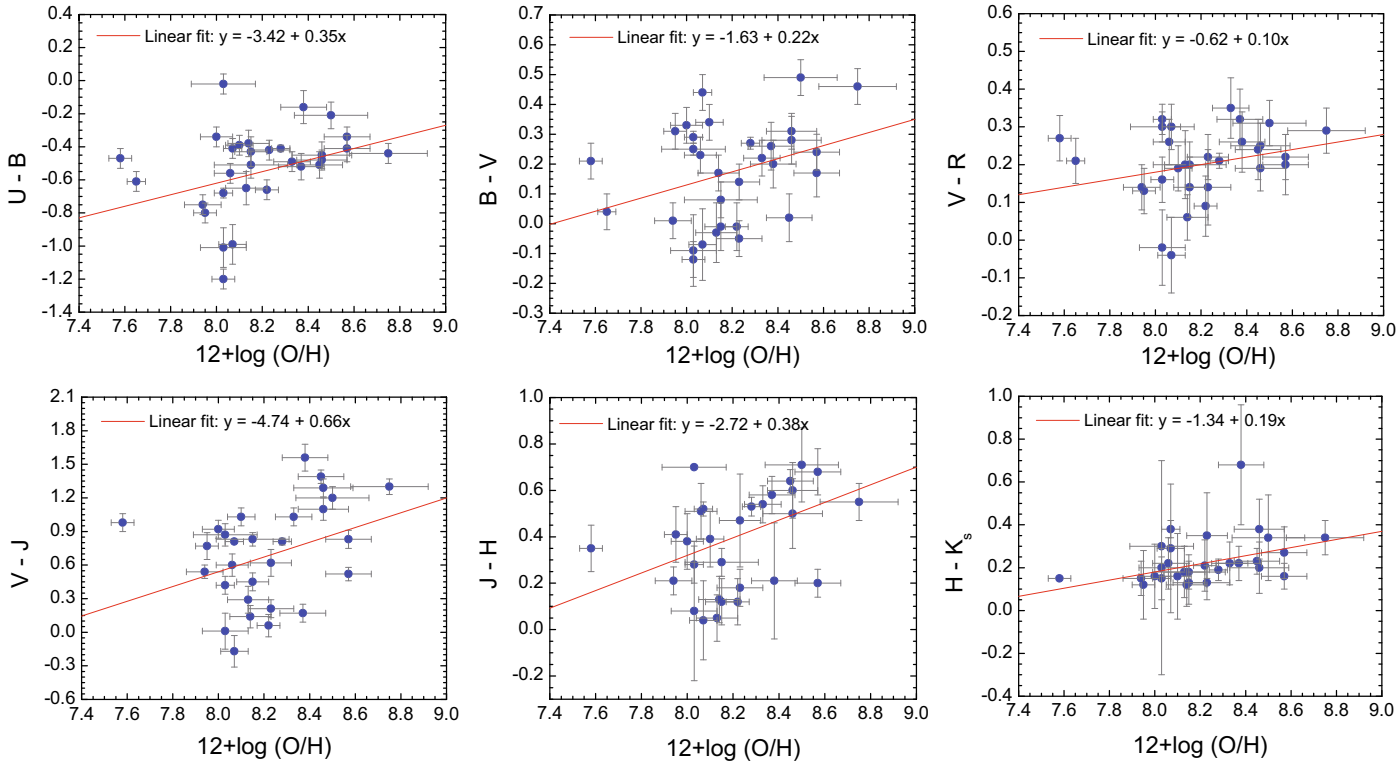

Fig. 19. Metallicity–colour diagrams for the galaxies analysed in this work. A linear fit is shown with a continuous red line.

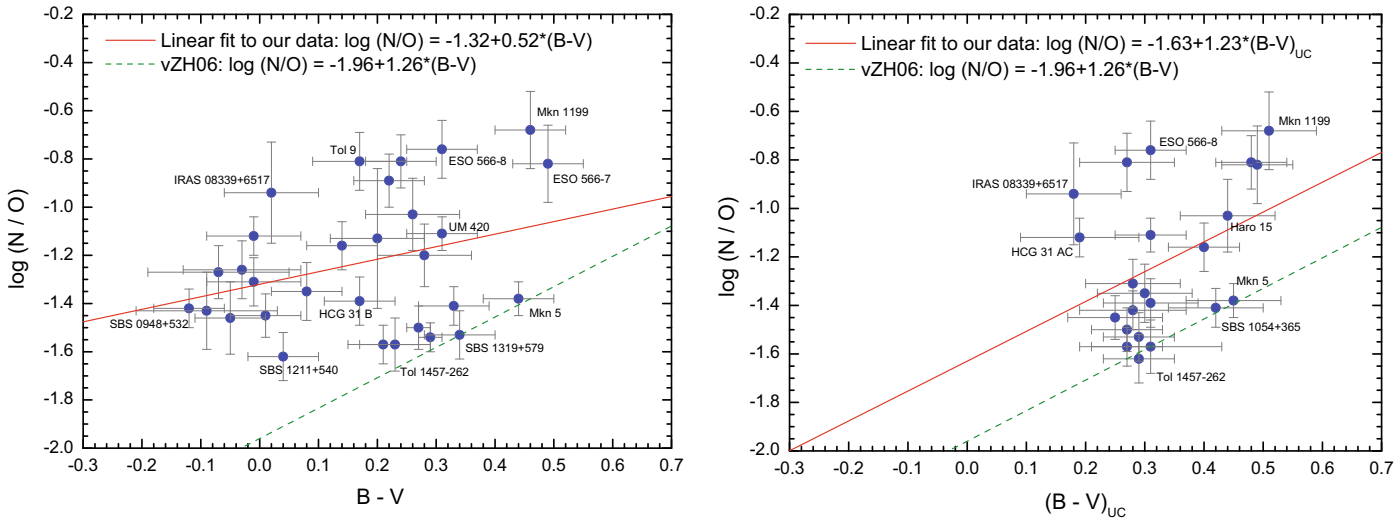

Fig. 20. N/O ratio vs. the reddening-corrected $B - V$ colour considering all the galaxy (left) or just the underlying stellar population (right). A linear fit to our data is shown with a continuous red line. The relationship found by van Zee & Haynes (2006) in their analysis of dwarf irregular galaxies is plotted with a dashed green line.

samples may be a consequence of two reasons: (i) we are comparing different objects – our sample is composed by starbursting galaxies, many of them BCDGs, but van Zee & Haynes (2006) analysed quiescent dwarf irregular galaxies with star-formation histories that are correctly modelled by simple changes in the SFR – and (ii) the N/O ratios tabulated by these authors, who used McGaugh (1991) photoionization models in many cases, are not well estimated – as we saw before, these models overestimate the oxygen abundance, and hence underestimate the N/O ratio, as it is clearly seen in the O/H–N/O diagram (Fig. 11, right) when comparing the van Zee et al. (1998) sample with the results provided by other authors –. We consider that the first reason may be the most reasonable explanation: objects with different star-formation histories have different relationships between the N/O ratio and other global characteristics such as optical colours.

However, as we commented before, using the B-magnitude may be not ideal to compare the colours and the chemical properties of these galaxies. Hence we also compared the N/O ratio with other optical and *NIR* colours, two of them ($V-R$ and $J-H$) are shown in Fig. 21. As we already explained when analysing the N/H–L relationship (Fig. 18), there are two kinds of objects with similar optical luminosities but with different nitrogen abundances. This is also reflected in the N/O ratio (Fig. 20, left), where normal and dwarf non-starbursting galaxies show a

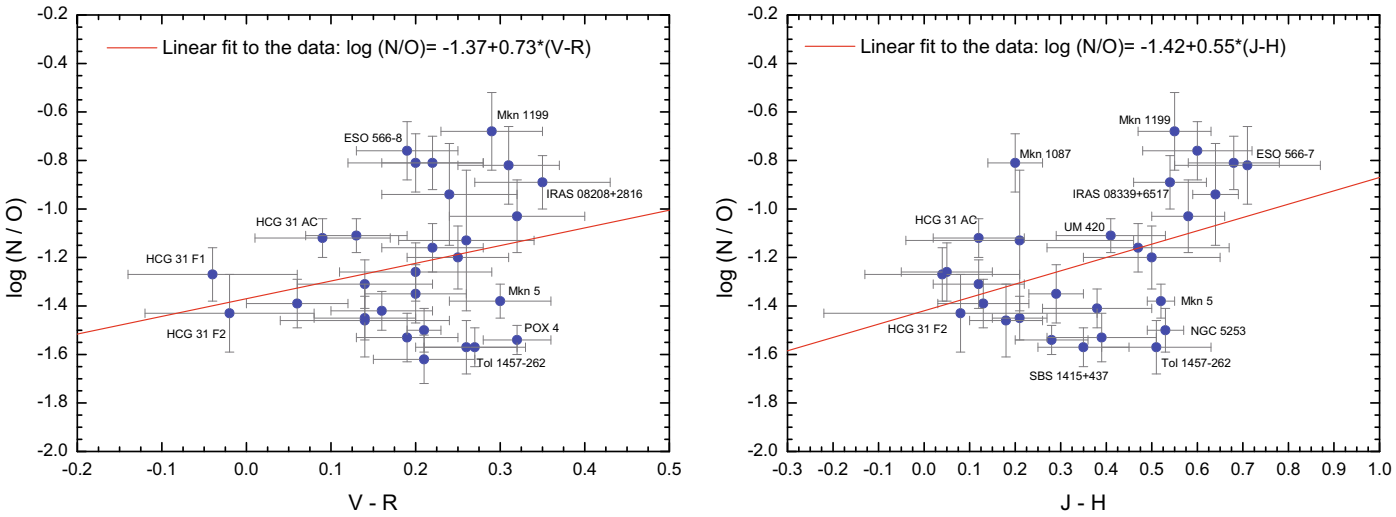

Fig. 21. N/O ratio vs. the reddening-corrected $V - R$ (*left*) and $J - H$ (*right*) colours. A linear fit to our data is shown with a continuous red line.

higher N/O ratio than starbursts (which have a lower N/O ratio in Fig. 20, left). This segregation is not so evident when comparing the N/O ratio with the *NIR* luminosities (Fig. 21, right), perhaps because the underlying component makes a higher contribution to the *NIR* magnitudes, but more data are needed to quantify this effect.

Finally, we also note that we do not see any clear relationship between the underlying population colours and the N/O ratio: for example, the $V - R$ colour of the low luminosity component is 0.31 ± 0.05 for all ranges of N/O. It was not possible to analyse the *NIR* colours of the low-luminosity component in the majority of the cases (see Table 5 in Paper I), but for the few available data it also seems that they are metallicity-independent, showing $J - H \sim 0.5 \pm 0.1$ and $H - K_S \sim 0.2$.

7. Conclusions

We compiled and analysed globally the optical/*NIR* colours and the physical and chemical properties of the ionized gas for a sample of 20 Wolf-Rayet galaxies. The individual analysis of the photometry of each galaxy was presented in Paper I, while the individual spectroscopic analysis was discussed in Paper II. The metallicity of these galaxies lies between 7.58 and 8.75 – in units of $12 + \log(O/H)$ –. The most important conclusions found in this study are

1. The colours estimated for our galaxy sample, which were corrected for both extinction and nebular emission using our spectroscopic data, agree quite well with the predictions given by evolutionary synthesis models, especially in compact and dwarf objects. Small discrepancies are explained because of the existence of several stellar populations within each galaxy and differences in their star-formation history. All galaxies show evidence of an old stellar population underlying the starburst, with ages older than 500 Myr.
2. We checked that all objects can be classified as pure star-forming galaxies. In total, we compiled 41 independent star-forming regions, of which 31 have a direct estimate of the electron temperature of the ionized gas, and hence their element abundances were derived using the direct method. We found that younger bursts have larger ionization budgets and are therefore capable to heat the ionized gas to higher electron temperatures. Both $c(H\beta)$ and W_{abs} increase with increasing metallicity, as predicted by galaxy evolution models.
3. We compiled the oxygen abundance and N/O, S/O, Ne/O, Ar/O, and Fe/O ratios in our WR galaxy sample. They generally agree well with previous observations. The N/O ratio is found to be rather constant for objects with $12 + \log(O/H) \leq 7.6$, has an important dispersion in galaxies with $7.6 \leq 12+\log(O/H) \leq 8.3$, and increases with the metallicity in objects with $12 + \log(O/H) \geq 8.3$. This behaviour is explained assuming the very different star-formation histories that each individual system has experienced.
4. We detected a high N/O ratio in objects showing clear WR features (HCG 31 AC, UM 420, IRAS 0828+2816, III Zw 107, ESO 566-8 and NGC 5253). The ejecta of the WR stars may be the origin of the N enrichment in these galaxies, but further detailed data comparing the chemical properties of a larger sample of both WR and non-WR galaxies, as well as careful analyses of galaxies showing a localized high N/O ratio, are needed.
5. The relative abundance ratios of the α-elements to oxygen are approximately constant, which is expected because all four elements are mainly produced by massive stars. We found indications of a moderate depletion of oxygen and iron onto grains in the most metal-rich galaxies.
6. We compared the abundances provided by the direct method with those obtained using the most common empirical calibrations:
   - the Pilyugin-method of Pilyugin (2001a,b), which considers the R_{23} and the P parameters and is updated by Pilyugin & Thuan (2005), is nowadays the best suitable empirical calibration to derive the oxygen abundance of star-forming galaxies. The cubic fit to R_{23} provided by Nagao et al. (2006) is not valid for analysing these star-forming galaxies;
   - the relations between the oxygen abundance and the N_2 or the O_3N_2 parameters provided by Pettini & Pagel (2004) give acceptable results for objects with $12 + \log(O/H) > 8.0$;
   - the results provided by empirical calibrations based on photoionization models (McGaugh 1991; Kewley & Dopita 2002; Kobulnicky & Kewley 2004) are systematically 0.2–0.3 dex higher than the values derived from the direct method. These differences are of the same

order as the abundance discrepancy found between abundances determined from recombination and collisionally excited lines of heavy-element ions. This may suggest temperature fluctuations in the ionized gas, as they exist in Galactic and other extragalactic H II regions.

7. We studied the optical/*NIR* luminosity–metallicity relations for our sample galaxies. We found that our data generally disagree with previous relations, perhaps because the objects analysed here host strong starbursts, but maybe also because we used the direct method and not the empirical calibrations to derive the oxygen abundances. The *L*–*Z* relations tend to be tighter when using *NIR* luminosities, TDG candidates are indeed easier detected using the M_{Ks}–*Z* relation.
8. The nitrogen abundance also has a strong correlation with the luminosity, but normal and dwarf non-starbursting galaxies show a higher N/O ratio than strong starbursting galaxies.
9. We found that galaxies with redder colours tend to have a higher oxygen abundance. The N/O ratio also increases with redder colours. Both results agree with galaxy evolution models. The colours of the underlying component seem to be metallicity-independent, but more data are still needed to confirm this trend.

We finally conclude that it is fundamental to perform a detailed analysis of both the photometric (optical and *NIR* magnitudes and colours of both burst and underlying component) and the chemical (oxygen abundances, N/O ratios) properties of these star-forming galaxies to understand the evolutionary stage of every system. A larger galaxy sample following the ideas compiled in this work will complement the results derived from huge databases (which do not distinguish the evolutionary state of the galaxies or the relative contribution of the burst/underlying populations, and for which the majority of the properties have been derived automatically and, in many cases, have considered empirical calibrations to determine the chemical abundances) when analysing the global properties and evolution of star-forming galaxies.

Acknowledgements. Á.R. L.-S. thanks C.E. (his formal PhD supervisor) for the help and very valuable explanations, talks and discussions during these years. He also acknowledges the help and support given by the Instituto de Astrofísica de Canarias (Spain) while doing his PhD. Á.R. L.-S. deeply thanks the Universidad de La Laguna (Tenerife, Spain) for force him to translate his PhD thesis from English to Spanish; he had to translate it from Spanish to English to complete this publication. This was the main reason of the delay of the publication of this research, because the main results shown here were already included in the PhD dissertation (in Spanish) which the first author finished in 2006 (López-Sánchez 2006). Á.R. L.-S. also thanks the people at the CSIRO/Australia Telescope National Facility, especially Bärbel Koribalski, for their support and friendship while translating his PhD. We are grateful to Janine van Eymeren for her comments about this manuscript, and to Mercedes Mollá for very fruitful discussions about the chemical evolution of the galaxies. We are also grateful for the comments provided by an anonymous referee, which improved the quality of this research. The authors also thank the language editor, A. Peter. This work has been partially funded by the Spanish Ministerio de Ciencia y Tecnología (MCyT) under project AYA2004-07466. This research has made use of the NASA/IPAC Extragalactic Database (NED) which is operated by the Jet Propulsion Laboratory, California Institute of Technology, under contract with the National Aeronautics and Space Administration. This research has made extensive use of the SAO/NASA Astrophysics Data System Bibliographic Services (ADS).

References

Alloin, D., Collin-Souffrin, S., Joly, M., & Vigroux, L. 1979, A&A, 78, 200
Amorín, R. O., Muñoz-Tuñón, C., Aguerri, J.A.L., Cairós, L.M., & Caon, N. 2007, A&A, 467, 541
Amorín, R., Aguerri, J. A. L., Muñoz-Tuñón, C., & Cairós, L. M. 2009, A&A, 501, 75
Bell, E. F., & de Jong, R. S. 2000, MNRAS, 312, 497
Bergvall, N., & Östlin, G. 2002, A&A, 390, 891
Bomans, D. J., van Eymeren, J., Dettmar, R.-J., Weis, K., & Hopp, U. 2007, NewAR, 51, 141
Boselli, A., Gavazzi, G., Donas., J., & Scodeggio, M. 2001, AJ, 121, 753
Bothun, G. D., Romanishin, W., Strom, S. E., & Strom, K. M. 1984, AJ, 89, 1300
Brinchmann, J., Kunth, D., & Durret, F. 2008, A&A, 485, 657
Bruzual, G., & Charlot, S. 2003, MNRAS, 344, 1000, BC03
Cairós, L.M., Vílchez, J.M., González Pérez, J.N., Iglesias-Páramo, J., & Caon, N. 2001a, ApJS, 133, 321
Cairós, L. M., Caon, N., Vílchez, J. M., González-Pérez, J. N., & Muñoz-Tuñón, C. 2001b, ApJS, 136, 393
Campos-Aguilar, A., Moles, M., & Masegosa, J. 1993, AJ, 106 1784
Clayton, D. D., & Pantelaki, I. 1993, PhR, 227, 293
Crowther, P. A. 2007, ARAA, 45, 177
Crowther, P. A., & Hadfield, L. J., 2006, A&A, 449, 711
Davé, R., & Oppenheimer, B. D. 2007, MNRAS, 374, 427
De Lucia, G., Kauffmann, G., & White, S. D. M. 2004, MNRAS, 374, 323
Denicoló, G., Terlevich, R., & Terlevich, E. 2002, MNRAS, 330, 69
de Naray, R. K., McGaugh S. S., & de Blok W. J. G., 2004, MNRAS, 355, 887
De Rossi, M. E., Tissera, P. B., & Scannapieco, C. 2006, MNRAS, 374, 323
Díaz, A. I., & Pérez-Montero, E. 2000, MNRAS, 312, 130
Dopita, M. A., & Evans, I. N. 1986, ApJ, 307, 431
Dopita, M. A., Kewley, L. J., Heisler, C. A., & Sutherland, R. S. 2000, ApJ, 542, 224
Dubois, Y., & Teyssier, R. 2007, EAS, 24, 95
Duc, P.-A., & Mirabel, I. F. 1998, A&A 338, 813
Duc, P. A., Brinks, E., Springel, V., Pichardo, B., Weilbacher, P., & Mirabel, I.F. 2000, AJ, 120, 1238
Edmunds, M. G., & Pagel, B. E. J. 1978, MNRAS, 185, 77
Edmunds, M. G., & Pagel, B. E. J. 1984, MNRAS, 211, 507
Erb, D. K., Shapley, A. E., Steidel, C. C., et al. 2003, ApJ, 591, 101
Erb, D. K., Shapley, A. E., Pettini, M., et al. 2006, ApJ, 644, 813
Esteban, C., & Peimbert, M. 1995, A&A, 300, 78
Esteban, C., Bresolin, F., Peimbert, M., et al. 2009, ApJ, 700, 654
Ferland G. J., Korista K. T., Verner D. A., et al. 1998, PASP, 110, 761
Fioc, M., & Rocca-Volmerange, B. 1997, A&A 326, 950
Gallagher, S. C., Durrell, P. R., Elmegreen, D. M., et al. 2010, AJ, 139, 545
García-Rojas, J., & Esteban, C., 2007, ApJ, 670, 457
Garnett, D. R. 1992, AJ, 103, 1330
Garnett, D. R. 2002, ApJ, 581, 1019
Hägele, G. F., Díez, Á. I., Terlevich, E., et al. 2008. MNRAS, 383, 209
Henry, R. B. C., Edmunds, M. G., & Köppen, J. 2000, ApJ, 541, 660
Hidalgo-Gámez, A. M., & Olofsson, K. 1998, A&A, 334, 45
Hirashita, H., Inoue, A. K., Kamaya, H., & Shibai, H. 2001, A&A, 366, 83
Izotov, Y. I., & Thuan, T. X. 1998, ApJ, 500, 188
Izotov, Y. I., & Thuan, T. X. 1999, ApJ, 511, 639
Izotov, Y. I., & Thuan, T. X. 2004, ApJ, 616, 768
Izotov, Y. I., Papaderos, P., Guseva, N. G., Fricke, K. J., & Thuan, T. X. 2004, A&A 421, 539
Izotov, Y. I., Stasińska, G., Meynet, G., Guseva, N. G., & Thuan, T. X. 2006, A&A, 448, 955
James, B. L., Tsamis, Y. G., & Barlow, M. J. 2010, MNRAS, 401, 759
Jansen, R. A., Franx, M., Fabricant, D., & Caldwell, N. 2000, ApJS, 126, 271
Jensen E. B., Strom K. M., & Strom S. E. 1976, ApJ, 209, 748
Kauffmann, G., & White, S. D. M. 1993, MNRAS, 261, 921
Kauffmann, G., Heckman, T. M., Tremonti, C., et al. 2003, MNRAS, 346, , 1055
Kennicutt, R. C. Jr., Bresolin, F., & Garnett, D. R. 2003, ApJ, 591, 801
Kewley, L. J., & Dopita, M. A. 2002, ApJS, 142, 35
Kewley, L. J., & Ellison, S. E. 2008, ApJ, 681, 1183
Kewley, L. J., Dopita, M. A., Sutherland, R. S., Heisler, C. A., & Trevena, J. 2001, ApJS, 556, 121
Kinman, T. D., & Davidson, K. 1981, ApJ, 243, 127
Kobulnicky, H. A., & Kewley, L. J. 2004, ApJ, 617, 240
Kobulnicky, H. A., & Skillman, E. D. 1998, ApJ, 497, 601
Kobulnicky, H. A., Skillman, E. D., Roy, J.-R., Walsh, J. R., & Rosa, M. R., 1997, ApJ, 277, 679
Kobulnicky, H. A., Kennicutt, R. C.Jr., & Pizagno, J. L. 1999, ApJ, 514, 544
Kobulnicky, H. A., Willmer, C. N. A., Phillips, A. C., et al. 2003, ApJ, 599, 1006
Lee, J. C., Salzer J. J., & Melbourne, J. 2004, ApJ, 616, 752
Leitherer, C., Schaerer, D., Goldader, J. D., et al. 1999, ApJS, 123, 3 (STARBURST 99)
Lequeux, J., Peimbert, M., Rayo, J. F., Serrano, A., & Torres-Peimbert, S. 1979, A&A, 80, 155
Liang, Y. C., Yin, S. Y., Hammer, F., et al. 2006, ApJ, 652, 257
Lilly, S. J., Carollo, C. M., & Stockton, A. N. 2003, ApJ, 597, 730
López-Sánchez, Á. R. 2006, Ph.D. Thesis, Universidad de la Laguna, Tenerife, Spain

López-Sánchez, Á. R., & Esteban, C. 2008, A&A, 491, 131, Paper I
López-Sánchez, Á. R., & Esteban, C. 2009, A&A, 508, 615, Paper II
López-Sánchez, Á. R., & Esteban, C. 2010, A&A, 516, 104, Paper III
López-Sánchez, Á. R., Esteban, C., & Rodríguez, M. 2004a, ApJS, 153, 243
López-Sánchez, Á. R., Esteban, C., & Rodríguez, M. 2004b, A&A, 428, 445
López-Sánchez, Á. R., Esteban, C., & García-Rojas, J. 2006, A&A, 449, 997
López-Sánchez, Á. R., Esteban, C., García-Rojas, J., Peimbert, M., & Rodríguez, M. 2007, ApJ, 656, 168
Mac Low, M., & Ferrara, A. 1999, ApJ, 513, 142
Marlowe, A. T., Heckman, T. M., Wyse, R. F. G., & Schommer, R. 1995, ApJ, 438, 563
Martín-Manjón, M. L., Mollá, M., Díaz, A. I., & Terlevich, R. 2008, MNRAS, 385, 854
McCall, M. L., Rybski, P. M., & Shields, G. A. 1985, ApJS 57, 1
McGaugh, S. S. 1991, ApJ, 380, 140
McGaugh, S. S. 1994, ApJ, 426, 135
McGaugh, S. S., & de Blok, W. J. G. 1997, ApJ, 481, 689
Mendes de Oliveira, C. L., Temporin, S., Cypriano, E. S., et al. 2006, AJ, 132, 570
Méndez, D. I., & Esteban, C. 1997, ApJ, 488, 652
Meynet, G., & Maeder, A. 2005, A&A, 429, 581
Mollá, M., Vílchez, J. M., Gavilán, M., & Díaz, A. I. 2006, MNRAS, 372, 1069
Nagao, T., Maiolino, R., & Marconi, A. 2006, A&A, 459, 85
Oey M. S., & Shields J. C. 2000, ApJ, 539, 687
Pagel, B. E. J., Edmunds, M. G., Blackwell, D. E., Chun, M. S., Smith, G. 1979, MNRAS, 189, 95
Papaderos, P., Guseva, N. G., Izotov, Y. I., et al. 2006, A&A, 457, 45
Peimbert, M. 1967, ApJ, 150, 825
Peimbert, M., Peimbert, A., Esteban, C., et al. 2007, RMxAC, 29, 72
Peña, M., & Ayala, S. 1993, Rev. Mex. Astron. Astrofis., 27, 171
Pérez-Montero, E., & Díaz, A. I. 2005, MNRAS, 361, 1063
Pettini, M., & Pagel, B. E. J. 2004, MNRAS, 348, 59
Pettini, M., Shapley, A. E., Steidel, C. C., et al. 2001, ApJ, 554, 981
Pilyugin, L. S. 2000, A&A, 362, 325
Pilyugin, L. S. 2001a, A&A, 369, 594
Pilyugin, L. S. 2001b, A&A, 374, 412
Pilyugin, L. S., & Thuan, T. X. 2005, ApJ, 631, 231
Pilyugin, L. S., Thuan, T. X., & Vílchez, J. M. 2003, A&A, 397, 487
Pilyugin, L. S., Vílchez, J. M., & Contini, T. 2004, A&A, 425, 849
Piovan, L., Tantalo, R., & Chiosi, C. 2006, MNRAS, 366, 923
Pustilnik, S., Kniazev, A., Pramskij, A., et al. 2004, A&A, 419, 469
Richer, M. G., & McCall, M. L. 1995, ApJ, 445, 642
Rubin, V. C., Ford, W. K., Jr., & Whitmore, B. C. 1984, ApJ, 281, L21
Salzer, J. J., Lee, J. C., Melbourne, J., et al. 2005, ApJ, 624, 661
Schaerer, D., & Vacca, W. D. 1998, ApJ, 497, 618 (SV98)
Schaerer, D., Contini, T., & Pindao, M. 1999, A&AS, 136, 35
Skillman, E. D., Kennicutt, R. C., & Hodge, P. W. 1989, ApJ, 347, 875
Springel, V., & Hernquist, L. 2003, MNRAS, 339, 312
Springel, V., White, S., Jenkins, A., et al. 2005, Nature, 435, 629
Stasińska, G. 2002, RMxAC, 12, 62
Stasińska, G. 2005, A&A, 434, 507
Stasińska, G. 2006, A&A, 454, 127
Stasińska, G. 2010, Stellar Populations – planning for the next decade, ed. Bruzual, & Charlot, Proc. IAU Symp., 262, 93
Stasińska, G., Schaerer, D., & Leitherer, C. 2001, A&A, 370, 1
Steidel, C. C., Shapley A. E., Pettini M., et al. 2004, ApJ, 604, 534
Storchi-Bergmann, T., Calzetti, D., & Kinney, A. L. 1994, ApJ, 429, 572
Sutherland, R. S., & Dopita, M. A. 1993, ApJS, 88, 253
Tenorio-Tagle, G., Muñoz-Tuñón, C., Pérez, E. Silich, S., & Telles, E. 2006, ApJ, 643, 186
Teplitz, H. I., Malkan, M. A., Steidel, C. C., et al. 2000, ApJ, 542, 18
Tissera, P. B., De Rossi, M. E., & Scannapieco, C. 2005, MNRAS, 364, L38
Torres-Peimbert, S., Peimbert, M., & Fierro, J. 1989, ApJ, 345, 186
Tremonti, C. A., Heckman, T. M., Kauffmann, G., et al. 2004, ApJ, 613, 898
van Eymeren, J., Bomans, D. J., Weis, K., & Dettmar, R.-J. 2007, A&A, 474, 67
van Eymeren, J., Marcelin, M., Koribalski, B. S., et al. 2009, A&A, 505, 105
van Eymeren, J., Koribalski, B. S., López-Sánchez, Á. R., Dettmar, R.-J., & Bomans, D. J. 2010, MNRAS, accepted
van Zee, L., Salzer, J. J., & Haynes, M. P. 1998, ApJ, 497, 1
van Zee, L., & Haynes, M.P. 2006, ApJ, 636, 214
Vázquez, G. A., & Leitherer, C. 2005, ApJ, 621, 695
Verma, A., Lutz, D., Sturm, E., et al. 2003, A&A, 403, 829
Vila-Costas, M. B., & Edmunds, M. G. 1992, MNRAS, 259, 121
Vila-Costas, M. B., & Edmunds, M. G. 1993, MNRAS, 265, 199
Vílchez, J. M., & Esteban, C. 1996, MNRAS, 280, 720
Weilbacher, P. M., Duc, P. A., & Fritze-von Alvensleben, U. 2003, A&A, 397, 545
Woosley S. E., & Weaver, T. A. 1995, ApJS, 101, 181
Wyse, R. F. G., & Silk, J. 1985, ApJ, 296, L1
Yin, S. Y., Liang, Y. C., Hammer, F., et al. 2007, A&A, 462, 535
York, D. G., Adelman, J., Anderson, J. E., Jr., et al. 2000, AJ, 120, 1579
Zaritsky, D., Kennicutt, R. C. Jr., & Huchra, J. P. 1994, ApJ, 420, 87

Pages 24 to 28 are available in the electronic edition of the journal at http://www.aanda.org

Appendix A: Empirical calibrations of the oxygen abundance

When the spectrum of an extragalactic H II region does not show the [O III] λ4363 emission line or other auroral lines that can be used to derive T_e, the so-called *empirical calibrations* are applied to get a rough estimation of its metallicity. Empirical calibrations are inspired partly by photo-ionization models and partly by observational trends of line strengths with galactocentric distance in gas-rich spirals, which are believed to be due to a radial abundance gradient with abundances decreasing outwards. In extragalactic objects, the usefulness of the empirical methods goes beyond the derivation of abundance gradients in spirals (Pilyugin et al. 2004), as these methods find application in chemical abundance studies of a variety of objects, including low-surface brightness galaxies (de Naray et al. 2004) and star-forming galaxies at intermediate and high redshift, where the advent of 8–10 m class telescopes has made it possible to extend observations (e.g., Teplitz et al. 2000; Pettini et al. 2001; Kobulnicky et al. 2003; Lilly et al. 2003; Steidel et al. 2004; Kobulnicky & Kewley 2004; Erb et al. 2006).

As the brightest metallic lines observed in spectra of H II regions are those involving oxygen, this element has been extensively used to get a suitable empirical calibration. Oxygen abundance is important as one of the fundamental characteristics of a galaxy: its radial distribution is combined with radial distributions of gas and star surface mass densities to constrain models of chemical evolution. Parameters defined in empirical calibrations evolving bright oxygen lines are

$$R_3 = \frac{I([\mathrm{O\,III}])\lambda4959 + I([\mathrm{O\,III}])\lambda5007}{\mathrm{H}\beta}, \quad (A.1)$$

$$R_2 = \frac{I([\mathrm{O\,II}])\lambda3727}{\mathrm{H}\beta}, \quad (A.2)$$

$$R_{23} = R_3 + R_2, \quad (A.3)$$

$$P = \frac{R_3}{R_{23}}, \quad (A.4)$$

$$y = \log\frac{R_3}{R_2} = \log\frac{1}{P^{-1}-1}. \quad (A.5)$$

Jensen et al. (1976) presented the first exploration in this method considering the R_3 index, which considers the [O III] $\lambda\lambda$4959,5007 emission lines. However, were Pagel et al. (1979) who introduced the most widely used abundance indicator, the R_{23} index, which also included the bright [O II] λ3727 emission line. Since then, many studies have been performed to refine the calibration of R_{23} (Edmunds & Pagel 1978; McCall et al. 1985; Dopita & Evans 1986; Torres-Peimbert et al. 1989; McGaugh 1991; Zaritsky et al. 1994; Pilyugin et al. 2000, 2001a,b; Kewley & Dopita 2002; Kobulnicky & Kewley 2004; Pilyugin & Thuan 2005; Nagao et al. 2006). The most successful are the calibrations of McGaugh (1991) and Kewley & Dopita (2002), which are based on photoionization models, and the empirical relations provided by Pilyugin (2001a,b) and Pilyugin & Thuan (2005). Both kinds of calibrations improve the accuracy by making use of the [O III]/[O II] ratio as ionization parameter, which accounts for the large scatter found in the R_{23} versus oxygen abundance calibration, which is larger than observational errors (Kobulnicky et al. 1999). Figure A.1 shows the main empirical calibrations that use the R_{23} parameter.

The main problem associated with the use of R_{23} parameter is that it is bivaluated, i.e., a single value of R_{23} can be caused by two very different oxygen abundances. The reason of this behaviour is that the intensity of oxygen lines *does not indefinitely increase* with metallicity. Thus, there are two *branches* for each empirical calibration (see Fig. A.1): the *low-metallicity* regime, with 12+log(O/H)≤8.1, and the *high-metallicity* regime, with 12+log(O/H)≥8.4. That means that a very large fraction of the star-forming regions lie in the ill-defined turning zone around 12+log(O/H) ≃ 8.20, where regions with the same R_{23} value have oxygen abundances that differ by almost an order of magnitude. Hence, additional information, such as the [N II]/Hα or the [O II]/[O III] ratios, is needed to break the degeneracy between the high and low branches (i.e., Kewley & Dopita, 2002). Besides, the R_{23} method requires that spectrophotometric data are corrected by reddening, which effect is crucial because [O II] and [O III] lines have a considerably separation in wavelength.

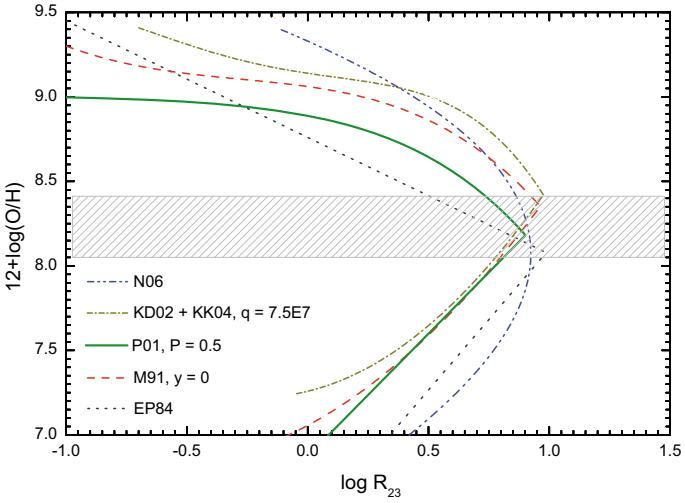

Fig. A.1. Empirical calibrations of oxygen abundance using the R_{23} parameter. Note that they are bi-valuated. The dashed zone indicates the region with higher uncertainties in O/H. The empirical calibrations plotted in the figure are: EP94: Edmunds & Pagel (1984); M91: McGaugh (1991) using $y = 0$ ($R_2 = R_3$); P01: Pilyugin (2001) using $P = 0.5$ ($R_2 = R_3$); (KD02+KK04): Kewley & Dopita (2002) using the formulation of Kobulnicky & Kewley (2004) assuming $q = 7.5 \times 10^7$ cm s^{-1}; N06: Nagao et al. (2006) using their cubic fit to R_{23}.

Here we list all empirical calibrations that were considered in this work, compiling the equations needed to derive the oxygen abundance from bright emission line ratios following every method.

Edmunds & Pagel (1984): Although the R_{23} parameter was firstly proposed by Pagel et al. (1979), the first empirical calibration was given by Edmunds & Pagel (1978),

$$\begin{aligned} 12 + \log(\mathrm{O/H})_{\mathrm{up}} &= 8.76 - 0.69\log R_{23}, \\ 12 + \log(\mathrm{O/H})_{\mathrm{low}} &= 6.43 + 1.67\log R_{23}, \end{aligned} \quad (A.6)$$

with the limit between the lower and the upper branches at 12 + log(O/H) ∼ 8.0.

McCall et al. (1985) presented an empirical calibration for oxygen abundance using the R_{23} parameter, only valid for 12+log(O/H) > 8.15. However, they did not give an analytic formulae but only listed it numerically (see their Table 15). The four-order polynomical fit for their values gives the following relation:

$$\begin{aligned} 12 + \log(\mathrm{O/H})_{\mathrm{up}} &= 9.32546 - 0.360465x + 0.203494x^2 \\ &\quad + 0.278702x^3 - 1.36351x^4, \end{aligned} \quad (A.7)$$

with $x = \log R_{23}$.

Table A.1. List of the parameters used to compute the oxygen abundance in all regions with a direct estimation of T_e using empirical calibrations.

Region	R_{23}	$P = R_3/R_{23}$	$y = \log(R_3/R_2)$	N_2	O_3N_2	q_{KD02o} [a]
HCG 31 AC	5.42	0.571	0.125	0.104	1.349	3.76E+07
HCG 31 B	7.93	0.408	–0.162	0.101	1.381	4.91E+07
HCG 31 E	7.12	0.511	0.020	0.090	1.486	7.40E+07
HCG 31 F1	8.91	0.819	0.656	0.034	2.201	5.78E+07
HCG 31 F2	7.60	0.724	0.418	0.036	2.064	6.28E+07
HCG 31 G	8.20	0.499	–0.002	0.106	1.462	6.96E+07
Mkn 1199 C	7.69	0.809	0.627	0.131	1.555	1.55E+08
Haro 15 A	9.73	0.884	0.881	0.027	2.378	8.55E+07
Mkn 5 A1	7.58	0.748	0.473	0.051	1.915	6.96E+07
Mkn 5 A2	8.19	0.702	0.372	0.049	1.944	1.72E+08
IRAS 08208+2816 C	7.77	0.793	0.583	0.129	1.558	8.55E+07
POX 4	10.68	0.906	0.986	0.015	2.697	1.05E+08
UM 420	6.45	0.649	0.268	0.099	1.497	4.81E+07
SBS 0926+606A	7.40	0.811	0.632	0.026	2.227	6.68E+07
SBS 0948+532	8.85	0.874	0.843	0.022	2.430	2.54E+08
SBS 1054+365	9.33	0.893	0.920	0.020	2.503	9.10E+07
SBS 1211+540	7.22	0.892	0.918	0.008	2.788	1.16E+08
SBS 1319+579A	9.92	0.908	0.996	0.014	2.671	1.05E+08
SBS 1319+579B	7.13	0.722	0.415	0.046	1.922	6.15E+07
SBS 1319+579C	7.11	0.710	0.389	0.052	1.860	5.91E+07
SBS 1415+437C	5.22	0.783	0.558	0.015	2.301	5.91E+07
SBS 1415+437A	4.86	0.810	0.629	0.012	2.370	5.44E+07
III Zw 107 A	7.13	0.701	0.369	0.100	1.573	5.78E+07
Tol 9 INT	4.58	0.689	0.345	0.252	0.973	4.16E+07
Tol 9 NOT	4.78	0.629	0.230	0.287	0.894	3.39E+07
Tol 1457-262A	9.89	0.773	0.532	0.033	2.236	9.91E+07
Tol 1457-262B	9.00	0.792	0.582	0.020	2.417	1.41E+08
Tol 1457-262C	8.88	0.669	0.359	0.036	2.099	7.16E+07
ESO 566-8	5.17	0.505	0.008	0.414	0.693	3.19E+07
NGC 5253 A	9.20	0.851	0.756	0.102	1.754	6.82E+07
NGC 5253 B	9.38	0.856	0.775	0.086	1.841	7.11E+07
NGC 5253 C	8.03	0.773	0.532	0.041	2.046	2.60E+08
NGC 5253 D	7.67	0.527	0.048	0.079	1.582	7.72E+07

Notes. [(a)] Value derived for the q parameter (in units of cm s^{-1}) obtained using the optimal calibration given by Kewley & Dopita (2002) .

Zaritsky et al. (1994) provided a simple analytic relation between oxygen abundance and R_{23}:

$$12 + \log(\mathrm{O/H})_{\mathrm{up}} = 9.265 - 0.33x - 0.202x^2 - 0.207x^3 - 0.333x^4. \quad \text{(A.8)}$$

Their formula is an average of three previous calibrations: Edmunds & Pagel (1978), McCall et al. (1985) and Dopita & Evans (1986). Following the authors, this calibration is only suitable for 12+log(O/H) > 8.20, but perhaps a more realistic lower limit is 8.35.

McGaugh (1991) calibrated the relationship between the R_{23} ratio and gas-phase oxygen abundance using H II region models derived from the photoionization code CLOUDY (Ferland et al. 1998). McGaugh's models include the effects of dust and variations in ionization parameter, y. Kobulnicky et al. (1999) give analytical expressions for the McGaugh (1991) calibration based on fits to photoionization models; the middle point between both branches is 12 + log(O/H) ∼ 8.4:

$$12 + \log(\mathrm{O/H})_{\mathrm{up}} = 7.056 + 0.767x + 0.602x^2 - y(0.29 + 0.332x - 0.331x^2), \quad \text{(A.9)}$$

$$12 + \log(\mathrm{O/H})_{\mathrm{low}} = 9.061 - 0.2x - 0.237x^2 - 0.305x^3 - 0.0283x^4 - y(0.0047 - 0.0221x - 0.102x^2 - 0.0817x^3 - 0.00717x^4). \quad \text{(A.10)}$$

Pilyugin (2000) found that the previous calibrations using the R_{23} parameter had a systematic error depending on the hardness of the ionizing radiation, suggesting that the excitation parameter, P, is a good indicator of it. In several papers, Pilyugin performed a detailed analysis of the observational data combined with photoionization models to obtain empirical calibrations for the oxygen abundance. Pilyugin (2000) confirmed the idea of McGaugh (1991) that the strong lines of [O II] and [O III] contain the necessary information for the determination of accurate abundances in low-metallicity (and may be also in high-metallicity) H II regions. He used new observational data to propose a linear fit involving only the R_{23} parameter,

$$12 + \log(\mathrm{O/H})_{\mathrm{up}} = 9.50 - 1.40 \log R_{23}, \quad \text{(A.11)}$$

$$12 + \log(\mathrm{O/H})_{\mathrm{low}} = 6.53 + 1.40 \log R_{23}, \quad \text{(A.12)}$$

Table A.2. Results of the oxygen abundance, in the form 12 + log(O/H), for objects with a direct estimation of the metallicity, considering several empirical calibrations.

Region	Branch	T_e	EP84	MRS85	M91	ZKH94	P00	P01[a]	PT05[b]	KD02	KK04	D02	PP04a	PP04b	PP04c	N06a[c]	N06b	N06c
			R_{23}	R_{23}	R_{23}, y	R_{23}	R_{23}	R_{23}, P	R_{23}, P	R_{23}, q	R_{23}, q	N_2	N_2	N_2	O_3N_2	R_{23}	N_2	O_3N_2
HCG 31 AC	H	8.22 ± 0.05	8.25	8.89	8.67	8.74	8.47	8.15	8.09	7.99	8.12	8.40	8.34	8.29	8.30	8.05	8.16	8.22
HCG 31 B	H	8.14 ± 0.08	8.14	8.48	8.29	8.44	8.24	8.22	8.12	8.41	8.44	8.39	8.33	8.28	8.29	8.07	8.16	8.20
HCG 31 E	H	8.13 ± 0.09	8.17	8.62	8.14	8.53	8.31	8.18	8.13	8.19	8.32	8.35	8.30	8.26	8.25	8.07	8.11	8.15
HCG 31 F1	L	8.07 ± 0.06	8.02	8.30	8.13	...	7.86	8.12	7.99	8.46	8.33	8.05	8.07	8.09	8.03	...	7.81	7.67
HCG 31 F2	L	8.03 ± 0.10	7.90	8.54	8.06	8.48	7.76	8.13	7.95	8.19	8.27	8.06	8.07	8.10	8.07	8.07	7.83	7.79
HCG 31 G	H	8.15 ± 0.08	8.13	8.43	8.26	8.40	8.22	8.11	8.17	8.31	8.42	8.41	8.34	8.29	8.26	8.07	8.17	8.16
Mkn 1199 C	H	8.75 ± 0.12	9.37	9.26	9.00	9.18	9.19	8.71	8.54	9.14	9.14	8.92	8.74	8.90	8.81	9.18	8.78	8.94
Haro 15 A	H	8.10 ± 0.06	8.08	...	8.14	...	7.91	8.12	8.12	8.48	8.34	7.98	8.01	8.05	7.97	...	7.74	7.38
Mkn 5 A1	L	8.07 ± 0.07	7.90	8.54	8.04	8.48	7.76	8.13	8.13	8.19	8.26	8.18	8.17	8.16	8.12	8.07	7.94	7.89
Mkn 5 A2	L	8.08 ± 0.07	7.95	8.43	8.14	8.41	7.81	7.92	8.17	8.18	8.33	8.16	8.15	8.15	8.11	8.07	7.92	7.87
IRAS 08208+2816	H	8.33 ± 0.08	8.15	8.50	8.55	8.46	8.25	8.42	8.35	8.35	8.25	8.47	8.39	8.34	8.23	8.35	8.23	8.11
POX 4	L	8.03 ± 0.04	8.15	...	8.20	...	7.97	7.92	8.06	8.48	8.40	7.78	7.86	7.91	7.87	...	7.53	...
UM 420	L	7.95 ± 0.05	7.78	8.73	7.98	8.61	7.66	7.85	7.86	8.02	8.16	8.20	8.39	8.33	8.28	7.57	8.15	8.14
SBS 0926+606A	L	7.94 ± 0.08	7.88	8.57	7.97	8.50	7.75	7.77	7.80	8.17	8.20	7.97	8.00	8.05	8.02	7.71	7.73	7.64
SBS 0948+532	L	8.03 ± 0.05	8.01	8.31	8.06	...	7.86	7.82	8.10	8.34	8.28	7.91	7.95	8.01	7.95	...	8.01	...
SBS 1054+365	L	8.00 ± 0.07	8.05	8.21	8.09	...	7.89	7.84	7.91	8.48	8.30	7.87	7.93	7.98	7.93	...	7.63	...
SBS 1211+540	L	7.65 ± 0.04	7.86	8.60	7.85	8.52	7.73	7.68	7.65	8.02	8.10	7.58	7.70	7.69	7.84	7.68	7.31	...
SBS 1319+579A	L	8.05 ± 0.06	8.09	...	8.13	...	7.93	8.11	8.11	8.48	8.33	7.77	7.85	7.90	7.88	...	7.52	...
SBS 1319+579B	L	8.12 ± 0.10	7.85	8.62	8.01	8.53	7.72	8.13	8.12	8.13	8.23	8.14	8.14	8.14	8.11	8.07	7.90	7.89
SBS 1319+579 C	L	8.15 ± 0.07	7.85	8.62	8.02	8.53	7.72	8.13	8.13	8.12	8.23	8.18	8.17	8.16	8.13	8.06	7.94	7.93
SBS 1415+437 C	L	7.58 ± 0.05	7.63	8.91	7.72	8.76	7.53	7.57	7.55	7.86	7.99	7.79	7.86	7.92	7.99	7.39	7.55	7.55
SBS 1415+437 A	L	7.61 ± 0.06	7.58	8.96	7.64	8.80	7.49	7.50	7.48	7.82	7.92	7.72	7.81	7.86	7.97	7.34	7.48	7.41
III Zw 107	H	8.23 ± 0.09	8.17	8.62	8.57	8.53	8.31	8.40	8.35	8.13	8.24	8.39	8.33	8.28	8.23	8.46	8.15	8.10
Tol 9 INT	H	8.58 ± 0.15	8.30	9.00	8.76	8.84	8.58	8.61	8.55	8.95	8.90	8.68	8.56	8.54	8.42	8.77	8.46	8.40
Tol 9 NOT	H	8.55 ± 0.16	8.29	8.97	8.73	8.81	8.55	8.56	8.50	8.94	8.88	8.72	8.59	8.59	8.44	8.75	8.51	8.44
Tol 1457-262A	L	8.05 ± 0.07	8.09	...	8.26	...	7.92	8.11	8.20	8.58	8.42	8.04	8.06	8.09	8.02	...	7.80	7.63
Tol 1457-262B	L	7.88 ± 0.07	8.55	...	8.21	...	7.87	7.91	8.21	8.38	8.29	7.88	7.93	7.99	7.96	...	7.60	...
Tol 1457-262C	L	8.06 ± 0.11	8.48	...	8.21	...	7.88	8.00	8.24	8.48	8.37	8.07	8.08	8.10	8.06	...	7.83	7.77
ESO 566-8	H	8.46 ± 0.11	8.27	8.92	8.68	8.77	8.50	8.44	8.38	8.92	8.84	8.84	8.68	8.76	8.51	8.70	8.66	8.53
NGC 5253 A	H	8.18 ± 0.04	8.09	8.24	8.13	...	8.15	8.11	8.13	8.53	8.33	8.40	8.34	8.28	8.17	...	8.16	8.00
NGC 5253 B	H	8.19 ± 0.04	8.09	8.21	8.14	...	8.14	8.11	8.13	8.48	8.34	8.34	8.29	8.25	8.14	...	8.10	7.94
NGC 5253 C	L	8.28 ± 0.04	8.14	8.46	8.53	8.42	8.23	8.38	8.32	8.67	8.63	8.11	8.11	8.13	8.08	8.30	7.87	7.80
NGC 5253 D	L	8.31 ± 0.07	8.15	8.52	8.19	8.47	8.26	8.23	8.17	8.32	8.37	8.31	8.27	8.23	8.22	8.37	8.07	8.10

Notes. The empirical calibrations and the parameters used for each of them are: EP84: Edmunds & Pagel (1984) that involves the R_{23} parameter; MRS85: McCall et al. (1985) using R_{23}; M91: McGaugh (1991) using R_{23} and y; ZKH94: Zaritsky et al. (1994) using R_{23}; P00: Pilyugin (2000) using R_{23}; P01: Pilyugin (2001a,b) using R_{23} and P; KD02: Kewley & Dopita (2002) using R_{23} and q; KK04: Kobulnicky & Kewley (2004) using R_{23} and q; D02: Denicoló et al. (2002) using the N_2 parameter; PP04: Pettini & Pagel (2004), using (a) N_2 with a linear fit, (b) N_2 with a cubic fit, (c) the O_3N_2 parameter; N06: Nagao et al. (2006) using the cubic relations involving the R_{23} (a), N_2 (b) and O_3N_2 (c) parameters. The value compiled in the column labeled T_e is the oxygen abundance derived by the direct method.

[a] The value listed for P01 is the average value between the high- and the low-metallicity branches for objects with $7.90 < 12 + \log(O/H) < 8.20$.

[b] The value listed for PT05 is the average value between the high- and the low-metallicity branches for objects with $8.05 < 12 + \log(O/H) < 8.20$.

[c] The value listed for N06 is the average value between the high- and the low-metallicity branches for objects with $8.00 < 12 + \log(O/H) < 8.15$.

assuming a limit of 12 + log(O/H) ∼ 8.0 between the two branches. This calibration is close to that given by Edmunds & Pagel (1978); it has the same slope, but Pilyugin (2000) is shifted towards lower abundances by around 0.07 dex. However, this new relation is not sufficient to explain the wide spread of observational data. Thus, Pilyugin (2001a) give the following, more real and complex, calibration involving also the excitation parameter P:

$$12 + \log(O/H)_{up} = \frac{R_{23} + 54.2 + 59.45P + 7.31P^2}{6.01 + 6.71P + 0.371P^2 + 0.243R_{23}}. \quad (A.13)$$

This is the so-called *P-method*, which can be used in moderately high-metallicity H II regions (12 + log(O/H) ≥ 8.3). Pilyugin used two-zone models of H II regions and assumed the T_e(O II) – T_e(O III) relation from Garnett (1992). For the low metallicity branch, Pilyugin (2001b) found that

$$12 + \log(O/H)_{low} = 6.35 + 1.45 \log R_{23} - 1.74 \log P. \quad (A.14)$$

Pilyugin estimates that the precision of oxygen abundance determination with this method is around 0.1 dex.

Pilyugin & Thuan (2005) revisited these calibrations including more spectroscopic measurements of H II regions in spiral and irregular galaxies with a measured intensity of the [O III] λ4363 line and recalibrate the relation between the oxygen abundance and the R_{23} and P parameters, yielding to:

$$12 + \log(O/H)_{low} = \frac{R_{23} + 106.4 + 106.8P - 3.40P^2}{17.72 + 6.60P + 6.95P^2 - 0.302R_{23}}, \quad (A.15)$$

$$12 + \log(\mathrm{O/H})_{\mathrm{up}} = \frac{R_{23} + 726.1 + 842.2P + 337.5P^2}{85.96 + 82.76P + 43.98P^2 + 1.793R_{23}}. \quad \text{(A.16)}$$

Kewley & Dopita (2002) used a combination of stellar population synthesis and photoionization models to develop a set of ionization parameters and abundance diagnostic based only on the strong optical emission lines. Their *optimal* method uses ratios of [N II], [O II], [O III], [S II], [S III] and Balmer lines, which is the full complement of strong nebular lines accessible from the ground. They also recommend procedures for the derivation of abundances in cases where only a subset of these lines is available. Kewley & Dopita (2002) models start with the assumption that R_{23}, and many of the other emission-line abundance diagnostics, also depends on the ionization parameter $q \equiv c \times U$, that has units of cm s^{-1}. They used the stellar population synthesis codes Starburst 99 (Leitherer et al. 1999; Vázquez & Leitherer 2005) and Pegase.2 (Fioc & Rocca-Volmerange 1997) to generate the ionizing radiation field, assuming burst models at zero age with a Salpeter IMF and lower and upper mass limits of 0.1 and 120 $M_{\odot}$, respectively, with metallicities between 0.05 and 3 times solar. The ionizing radiation fields were input into the photoionization and shock code, Mappings (Sutherland & Dopita 1993), which includes self-consistent treatment of nebular and dust physics. Kewley & Dopita (2002) previously used these models to simulate the emission-line spectra of H II regions and starburst galaxies (Dopita et al. 2000), and are completely described in their study.

Kobulnicky & Kewley (2004) gave a parameterization of the Kewley & Dopita (2002) R_{23} method with a form similar to that given by McGaugh (1991) calibration. Kobulnicky & Kewley (2004) presented an iterative scheme to resolve for both the ionization parameter q and the oxygen abundance using only [O III], [O II] and Hβ lines. The parameterization they give for q is

$$\begin{aligned}\log(q) = {} & \Big(32.81 - 1.153y^2 + \big[12 + \log(\mathrm{O/H})\big] \\ & \big[-3.396 - 0.025y + 0.1444y^2\big]\Big) \\ & \Big(4.603 - 0.3119y - 0.163y^2 + \big[12 + \log(\mathrm{O/H})\big] \\ & \big[-0.48 + 0.0271y + 0.02037y^2\big]\Big)^{-1}, \end{aligned} \quad \text{(A.17)}$$

where $y = \log([\mathrm{O\,III}]/[\mathrm{O\,II}])$. This equation is only valid for ionization parameters between $5{\times}10^6$ and $1.5{\times}10^8$ cm s^{-1}. The oxygen abundance is parameterized by

$$\begin{aligned}12 + \log(\mathrm{O/H})_{\mathrm{up}} = {} & 9.72 - 0.777x - 0.951x^2 \\ & - 0.072x^3 - 0.811x^4 - \log(q) \\ & \times\Big(0.0737 - 0.0713x - 0.141x^2 \\ & + 0.0373x^3 - 0.058x^4\Big), \end{aligned} \quad \text{(A.18)}$$

$$\begin{aligned}12 + \log(\mathrm{O/H})_{\mathrm{low}} = {} & 9.40 + 4.65x - 3.17x^2 \\ & - \log(q)\Big(0.272 + 0.547x - 0.513x^2\Big), \end{aligned} \quad \text{(A.19)}$$

being $x = \log R_{23}$. The first equation is valid for 12+log(O/H)≥8.4, while the second for 12+log(O/H)<8.4. Typically, between two and three iterations are required to reach convergence. Following the authors, this parameterization should be regarded as an improved, implementation-friendly approach to be preferred over the tabulated R_{23} coefficients given by Kewley & Dopita (2002).

Nagao et al. (2006) did not consider any ionization parameter. They merely used data of a large sample of galaxies from the SDSS to derive a cubic fit to the relation between R_{23} and the oxygen abundance,

$$\log R_{23} = 1.2299 - 4.1926y + 1.0246y^2 - 0.063169y^3, \quad \text{(A.20)}$$

with $y = 12 + \log(\mathrm{O/H})$.

Besides R_{23}, additional parameters have been used to derive metallicities in star-forming galaxies. Without other emission lines, the N_2 parameter, which is defined by

$$N_2 \equiv \log \frac{I([\mathrm{N\,II}])\lambda 6583}{\mathrm{H}\alpha}, \quad \text{(A.21)}$$

can be used as a crude estimator of metallicity. However, we note that the [N II]/Hα ratio is particularly sensitive to shock excitation or a hard radiation field from an AGN. The N_2 parameter was firstly suggested by Storchi-Bergmann et al. (1994), who gave a tentative calibration of the oxygen abundance using this parameter. This calibration has been revisited by van Zee et al. (1998); Denicoló et al. (2002); Pettini & Pagel (2004) and Nagao et al. (2006). The Denicoló et al. (2002) calibration is

$$12 + \log(\mathrm{O/H}) = 9.12 + 0.73\mathrm{N}_2, \quad \text{(A.22)}$$

which considerably improves the previous relations because of the inclusion of an extensible sample of nearby extragalactic H II regions. The uncertainty of this method is ~0.2 dex because N_2 is sensitive to ionization and O/N variations, so strictly speaking it should be used mainly as an indicator of galaxy-wide abundances. Denicólo et al. (2002) also compared their method with photoionization models, concluding that the observed N_2 is consistent with nitrogen being a combination of both primary and secondary origin.

Pettini & Pagel (2004) revisited the relation between the N_2 parameter and the oxygen abundance including new data for the high- and low-metallicity regimen. They only considered those extragalactic H II regions where the oxygen values are determined either via the T_{e} method or with detailed photoionization modelling. Their linear fit to their data is

$$12 + \log(\mathrm{O/H}) = 8.90 + 0.57N_2, \quad \text{(A.23)}$$

which has both a lower slope and zero-point that the fit given by Denicoló et al. (2002). A somewhat better relation is provided by a third-order polynomical fit of the form

$$\begin{aligned}12 + \log(\mathrm{O/H}) = {} & 9.37 + 2.032N_2 \\ & + 1.26(N_2)^2 + 0.32(N_2)^3, \end{aligned} \quad \text{(A.24)}$$

valid in the range $-2.5 < N_2 < -0.3$. Nagao et al. (2006) also provided a relation between N_2 and the oxygen abundance, their cubic fit to their SDSS data yields

$$\log N_2 = 96.641 - 39.941y + 5.2227y^2 - 0.22040y^3, \quad \text{(A.25)}$$

with $y = 12 + \log(\mathrm{O/H})$.

Pettini & Pagel (2004) revived the O_3N_2 parameter, previously introduced by Alloin et al. (1979) and defined by

$$\mathrm{O_3N_2} \equiv \log \frac{[\mathrm{O\,III}]\ \lambda 5007/\mathrm{H}\beta}{[\mathrm{N\,II}]\ \lambda 6583/\mathrm{H}\alpha}. \quad \text{(A.26)}$$

Pettini & Pagel (2004) derived the following least-square linear fit to their data:

$$12 + \log(\mathrm{O/H}) = 8.73 - 0.32\mathrm{O_3N_2}. \quad \text{(A.27)}$$

Nagao et al. (2006) also revisited this calibration and derived a cubic fit between the O_3N_2 parameter and the oxygen abundance,

$$\log O_3N_2 = -232.18 + 84.423y - 9.9330y^2 + 0.37941y^3, \quad \text{(A.28)}$$

with $y = 12 + \log(O/H)$.

Other important empirical calibrations that were not used in this study involve the S_{23} parameter, introduced by Vílchez & Esteban (1996) and revisited by Díaz & Pérez-Montero (2000); Oey & Shields (2000) and Pérez-Montero & Díaz (2005). In the last years, bright emission line ratios such as [Ar III]/[O III] and [S III]/[O III] Stasińska (2006) or [Ne III]/[O III] and [O III]/[O II] (Nagao et al. 2006) have been explored as indicators of the oxygen abundance in H II regions and starburst galaxies. Peimbert et al. (2007) suggested to use the oxygen recombination lines to get a more precise estimation of the oxygen abundance. Nowadays, there is still a lot of observational and theoretical work to do involving empirical calibrations (see recent review by Kewley & Ellison 2008), but these methods should be used only for objects whose H II regions have the same structural properties as those of the calibrating samples (Stasińska 2010).